

## Full paper

## Structurally disordered lithiophilic graphene via solid-state exfoliation enables reversible lithium deposition with fast kinetics



Wootaeck Choi <sup>a,1</sup>, Min Sung Kang <sup>b,c,1</sup>, Kwanghyun Kim <sup>d</sup>, Han Uk Lee <sup>b,c</sup>, Sung Beom Cho <sup>b,c,\*</sup>, Junghyun Choi <sup>e,\*\*</sup>, Patrick Joohyun Kim <sup>a,d,\*\*\*</sup>

<sup>a</sup> School of Semiconductor Convergence Engineering, Kyungpook National University, Daegu 41566, Republic of Korea

<sup>b</sup> Department of Materials Science and Engineering, Ajou University, Suwon-si 16499, Republic of Korea

<sup>c</sup> Department of Energy Systems Research, Ajou University, Suwon-si 16499, Republic of Korea

<sup>d</sup> School of Chemical Engineering and Applied Chemistry, Kyungpook National University, Daegu 41566, Republic of Korea

<sup>e</sup> School of Chemical, Biological and Battery Engineering, Gachon University, Seongnam-si, Gyeonggi-do 13120, Republic of Korea

## ARTICLE INFO

## ABSTRACT

## Keywords:

Graphite  
Solid-state exfoliation  
Fracture mechanism  
Lithiophilicity  
Lithium-metal batteries

Lithium (Li) metal batteries have attracted significant attention as next-generation energy storage systems due to the high theoretical capacity ( $3860 \text{ mAh g}^{-1}$ ) and low redox potential ( $-3.04 \text{ V vs. SHE}$ ) of Li metal. However, their commercialization has been hindered by critical challenges such as low coulombic efficiency and the formation of Li dendrites, which deteriorate cycling stability and safety. Herein, lithiophilic graphene (LG) is prepared via the solid-state exfoliation of graphite under an inert atmosphere, and the atomic defects generated during the exfoliation process are exploited as uniform lithiophilic sites in order to induce dense and homogeneous Li plating. Solid-state exfoliation under inert conditions promotes effective exfoliation due to the absence of oxygen-containing surface groups, which typically inhibit crack propagation, as further validated by molecular dynamics simulations. With the combined effects of lithiophilic defects and controlled particle size in the LG, both Li–Cu and anode-less cells employing LG-modified current collectors exhibit markedly enhanced capacity retention. Moreover, when employed as a coating layer on the separator of an Li–S battery, the LG delivers improved electrochemical performance. These findings highlight the potential of LG to facilitate dendrite-free Li deposition and long-term reversible electrochemical reactions in Li-metal based batteries.

## 1. Introduction

Lithium-ion batteries have played a central role in modern energy storage systems [1]. However, their limited energy density has driven extensive research toward alternative battery systems. Among the many candidate devices, lithium metal batteries (LMBs) have received significant attention because of the high theoretical capacity ( $3860 \text{ mAh g}^{-1}$ ) and low redox potential ( $-3.04 \text{ V vs. SHE}$ ) of metallic Li [2,3]. Despite these advantages, LMBs suffer from critical issues, including the growth of Li dendrites and the formation of unstable solid electrolyte interphases, both of which severely limit their long-term cycling performance and safety [4]. To address these limitations, various strategies have been investigated, including electrolyte modification by the

incorporation of functional additives or alternative solvents to stabilize interfacial reactions [5,6], separator engineering to regulate ionic flux and suppress dendrite growth [7,8], current collector design to facilitate uniform Li nucleation and deposition [9,10], and the introduction of protective interfacial layers on the Li metal anode to mitigate parasitic side reactions [11,12].

Among these approaches, the modification of separators and current collectors offers a practical advantage, as these strategies can be implemented without complex processing steps and can directly regulate the Li depositional morphology. Carbon-based materials are particularly attractive in current collectors and separator modification because they help to reduce local current density and facilitate uniform Li deposition during cycling [13,14]. However, one of the major

\* Corresponding author at: Department of Materials Science and Engineering, Ajou University, Suwon-si 16499, Republic of Korea.

\*\* Corresponding author.

\*\*\* Corresponding author at: School of Semiconductor Convergence Engineering, Kyungpook National University, Daegu 41566, Republic of Korea.

E-mail addresses: [csb@ajou.ac.kr](mailto:csb@ajou.ac.kr) (S.B. Cho), [junghchoi@gachon.ac.kr](mailto:junghchoi@gachon.ac.kr) (J. Choi), [pjkim@knu.ac.kr](mailto:pjkim@knu.ac.kr) (P.J. Kim).

<sup>1</sup> These authors contributed equally to this work.

drawbacks of carbon materials is their inherently low affinity toward Li, which often leads to inhomogeneous Li nucleation and uneven plating [15,16]. This non-uniform deposition can cause severe electrochemical issues, such as low coulombic efficiency (CE) and internal short circuits. To overcome the lithiophilicity limitation of carbon materials, various modification approaches have been explored [17–20]. For example, Huang *et al.* [20] used nitrogen doping to improve the Li affinity of graphene and achieve uniform deposition, while Choi *et al.* [7] enhanced the interfacial wettability of graphene-coated separators by incorporating hydrophilic surface coatings, thereby improving the cycling stability of Li–S batteries.

In this study, graphite is first subjected to solid-state exfoliation under ambient and inert atmospheres to examine the effect of environment on the exfoliation process. After that, the effects of graphite surface chemistry and structural characteristics on Li deposition and electrochemical reversibility in Li metal-based cells are systematically investigated. When solid-state exfoliation is performed under an air atmosphere, oxygen-containing functional groups are formed on the graphite surface, thereby suppressing the propagation of microcracks and reducing the exfoliation efficiency, thus resulting in reduced-size graphite (RGr). By contrast, when solid-state exfoliation is performed under an argon (Ar) atmosphere, the resulting lithiophilic graphene (LG) exhibits a smaller particle size, lower crystallinity, and higher degree of structural disorder due to the limited formation of oxygen functional groups. In addition, the mechanisms of crack propagation and structural evolution under the different atmospheric conditions are analyzed using molecular dynamics simulations. The results suggest that the introduction of atomic defects in LG substantially lowers the  $\text{Li}^+$  adsorption energy, thereby enabling more uniform lithiation during the initial stages of cycling. Given that carbon-based materials such as graphene tend to develop lithiophilic characteristics upon lithiation, this uniform lithiation is expected to facilitate more homogeneous and reversible Li plating in subsequent cycles [21–23]. The reduced particle size of LG shortens the  $\text{Li}^+$  transport pathways and increases the surface area, thereby providing more active sites and enhancing the interfacial kinetics. Moreover, the broad particle size distribution improves the coating uniformity by enabling dense and homogeneous particle packing, which supports electrode integrity and current distribution. Meanwhile, the expanded interlayer spacing in the LG reduces the steric hindrance for  $\text{Li}^+$  intercalation, thereby lowering the energy barrier and facilitating faster ion transport, particularly under high-rate conditions. These structural advantages of LG collectively contribute to its superior electrochemical performance, as evidenced by an improved cycling stability in Li–Cu cells and anode-less Li metal batteries (ALLMBs). Furthermore, when employed as a separator coating in an Li–S battery, the LG effectively confines polysulfide species within the cathodic region, thereby enhancing the cycling stability. These findings highlight the broad applicability of LG synthesized via a simple exfoliation process, thereby demonstrating its potential as a viable alternative to conventional graphene powder in various battery systems.

## 2. Materials and methods

### 2.1. Preparation of RGr and LG

Artificial graphite powder (MTI) was used as the starting material for the preparation of RGr and LG. To prepare the RGr, the graphite powder and stainless-steel balls were loaded into a stainless-steel milling container at a mass ratio of 20:1. The container was sealed under ambient air without any special atmospheric control and ball milling was performed at 500 rpm for 8 days. For the LG, all handling steps were performed in an Ar-filled glove box to prevent oxygen exposure. The graphite powder, stainless-steel container, and milling balls were first transferred into the glove box, after which the powder and balls were loaded into the container at the same mass ratio of 20:1. The container was then sealed inside the glove box and ball milling was performed

under identical conditions (500 rpm for 8 days).

### 2.2. Preparation of the current collectors and separators with graphite, RGr, LG

Coating slurries of graphite, RGr, and LG were prepared by dispersing 0.9 g of each material with 0.1 g of polyvinylidene fluoride (PVDF) binder in 1-methyl-2-pyrrolidone (NMP, 99.5 %, SAMCHUN). The mixtures were homogenized using a planetary mixer (AR-100, THINKY) at 2000 rpm for 10 min. The resulting slurries were each uniformly coated onto Cu foil via tape casting to a thickness of 18  $\mu\text{m}$  to obtain the graphite@Cu, RGr@Cu, and LG@Cu current collectors, or onto polypropylene (PP; Celgard 2400) to obtain the graphite@PP, RGr@PP, and LG@PP separators. After coating, the samples were dried overnight in a convection oven at 60 °C. The dried current collectors were then punched into 12 mm discs, and the separators into 18 mm discs for subsequent use in cell assembly.

### 2.3. Fabrication of Li–Cu cells, anode-less LFP cells, and Li–S cells

All electrochemical experiments were conducted using CR2032-type coin cells, and all cell assembly processes were conducted in an Ar-filled glove box with O<sub>2</sub> and H<sub>2</sub>O levels maintained below 0.1 ppm.

In the Li–Cu cell configuration, graphite@Cu, RGr@Cu, and LG@Cu current collectors were used, along with a PP separator, a 0.3 T Li metal foil, and an electrolyte consisting of 1.0 M LiPF<sub>6</sub> in a 1:1 vol% mixture of ethylene carbonate (EC) and diethyl carbonate (DEC).

For the anodeless LiFePO<sub>4</sub> (LFP) cells, the LFP cathode with an areal capacity of ~1.2 mAh cm<sup>-2</sup> was prepared by mixing 0.8 g of LFP, 0.1 g of Super P, and 0.1 g of PVDF, followed by tape casting. As part of the cell preparation, partial Li plating was performed on the current collectors before cycling. The cells were assembled using the graphite@Cu, RGr@Cu, or LG@Cu current collector, a PP separator, the as-prepared LFP electrode, and an electrolyte consisting of 1.15 M LiPF<sub>6</sub> in a 1:1:2 vol% mixture of ethylene carbonate (EC), diethyl carbonate (DEC), and dimethyl carbonate (DMC), with additives of 1 % vinylene carbonate (VC), 1 % Li difluorophosphate (LiPO<sub>2</sub>F<sub>2</sub>), and 12.5 % fluoroethylene carbonate (FEC).

For the assembly of full Li–S cells, the sulfur cathode was prepared by mixing 0.6 g of sulfur, 0.3 g of Super P, and 0.1 g of PVDF, followed by tape casting. The cells were assembled using the prepared sulfur cathode, along with the graphite@PP, RGr@PP, or LG@PP separator (thickness = 18  $\mu\text{m}$ ), an Li metal anode, and an electrolyte composed of 1.0 M Li bis(trifluoromethanesulfonyl)imide (LiTFSI) in a 1:1 vol% mixture of 1,3-dioxolane (DOL) and dimethoxyethane (DME), with LiNO<sub>3</sub> as an additive.

### 2.4. Characterization

The surface morphologies of the graphite, RGr, and LG samples were examined using a field-emission scanning electron microscope (FE-SEM; Hitachi SU8230) equipped with an energy-dispersive X-ray spectroscope (EDS; Ultim Max100, OXFORD). Prior to analyzing the Li plating behavior and dendrite formation, the assembled cells were disassembled in an Ar-filled glove box and rinsed with DEC to remove any residual Li salts. X-ray photoelectron spectroscopy (XPS) was performed using a Thermo Fisher NEXSA instrument to investigate the surface chemical composition. The Fourier transform infrared (FT-IR) spectra were recorded in the 600–4000  $\text{cm}^{-1}$  range using an IR Prestige-21 spectrometer (Shimadzu). The crystallographic structures of the materials were characterized by X-ray diffraction (XRD) using a Panalytical EMPYREAN diffractometer. Electrochemical performance tests were conducted using a CT-4008Q-5 V100 mA-124 battery cycler (Neware). Electrochemical impedance spectroscopy (EIS) was performed using a VSP system (Biologic, Seyssinet-Pariset) in the frequency range of 10 mHz to 200 kHz with an AC amplitude of 10 mV. The Li-ion diffusion

coefficient was evaluated by the galvanostatic intermittent titration technique (GITT) using a WBCS300L32 system (WonATech), in which a  $0.2 \text{ mA cm}^{-2}$  current pulse was applied within the voltage range of  $0.001\text{--}1.0 \text{ V vs. Li/Li}^+$  for 10 min, followed by a 10-min rest period. The wettability of each coating was assessed by measuring the contact angle using a Phoenix300 Touch goniometer (SEO). Particle size analysis (PSA) was performed using a Mastersizer 3000 analyzer (Malvern Instruments). The microstructure of each sample was examined using field-emission transmission electron microscopy (FE-TEM; Titan G2, FEI, USA). The Brunauer-Emmett-Teller (BET) surface area and pore-size distributions were determined from the nitrogen ( $\text{N}_2$ ) adsorption-desorption isotherms measured at 77 K using a gas adsorption analyzer (3-Flex, Micromeritics, GA), and the pore size distributions were derived by using the Barrett-Joyner-Halenda (BJH) model. The porosity analysis was conducted using a mercury intrusion porosimeter (Autopore V 9620, Micromeritics).

### 2.5. DFT calculations

Density functional theory (DFT) calculations were performed with the projector augmented wave (PAW) potentials [24] by using the VASP software package [25], and the precision of the implementation was assessed using the generalized gradient approximation (GGA) with the Perdew-Burke-Ernzerhof exchange-correlation functional [26]. The electronic wave functions were expressed using a plane wave basis set with a cut-off energy of 520 eV to minimize the Pulay stress during structural optimization. The structural optimization was truncated when the Hellmann-Feynman forces reached the threshold value of  $0.01 \text{ eV}/\text{\AA}$ . The two-dimensional Brillouin zone was sampled by using a  $2 \times 2 \times 1$  mesh of  $\Gamma$ -centered  $k$ -points. The adsorption energy per  $\text{Li}^+$  ion ( $E_{\text{ads}}$ ) is defined by Eq. (1):

$$E_{\text{ads}} = E_{\text{Graphene-Li}} - (E_{\text{Graphene}} + E_{\text{Li}}) \quad (1)$$

where  $E_{\text{Graphene-Li}}$ ,  $E_{\text{Graphene}}$ , and  $E_{\text{Li}}$  represent the total energies of the graphene with adsorbed  $\text{Li}^+$  ions, the free graphene, and a free  $\text{Li}^+$  ion, respectively.

### 2.6. Molecular dynamics simulations

Classical molecular dynamics simulations were performed by using the large-scale atomic/molecular massively parallel simulator (LAMMPS) package [27] to model graphene failure. The reactive force field potential (ReaxFF) developed by Chenoweth *et al.* was used to capture the bond dynamics and interatomic interactions between carbon, oxygen, and hydrogen atoms [28,29]. In all simulations, the nearest neighbor and hydrogen bond cut-off distances were set to 4.5 and 6 Å, respectively. A graphene sheet ( $27 \times 27 \text{ nm}$ ) with approximately 28,139 atoms in total was generated using Pymatgen [30], and a crack was manually introduced. The cracked graphene sheet was then functionalized with O and OH atoms at two different concentrations to model the Ar and air conditions. In-plane boundary conditions were imposed on the simulation box to eliminate the effects of the finite size and free edges. The system was relaxed at 300 K for 12.5 ps under the NPT ensemble [31]. Subsequently, tensile strain was applied along the y-direction at a strain rate of  $10^{-3} \text{ ps}^{-1}$  [32]. The timestep was set at 0.25 fs for all simulations. Uniaxial tensile loading conditions were achieved by applying the NPT ensemble with zero pressure in the direction perpendicular to loading on the simulation box. Additionally, charge equilibration was performed every 10 steps. The simulation trajectory was analyzed using the OVITO software during post-processing [33].

### 2.7. FEM simulations

The finite element method (FEM) was used to investigate the Li behavior in an asymmetric Li-Cu cell. The deposition process was

modeled using COMSOL Multiphysics 6.2, integrating both electrochemical and ion transport physics to capture the dynamics of Li deposition on the graphene surface.

#### 2.7.1. Species transport

The transport of diluted species  $i$  in the electrolyte is described by the mass balance equation, given here as Eq. (2):

$$\frac{\partial c_i}{\partial t} + \nabla \bullet J_i = 0 \quad (2)$$

where  $J_i$  is the flux of species  $i$ . The flux is given by the Nernst-Planck equation, which considers both diffusion and electromigration effects. In this model, convection is neglected, and the ionic flux is expressed as Eq. (3):

$$J_i = -D_i \nabla c_i - \frac{D_i z_i F}{k_B T} c_i \nabla \phi_l \quad (3)$$

where  $D_i$ ,  $c_i$ , and  $z_i$  represent the diffusion coefficient, ionic concentration, and valence charge of species  $i$ ,  $F$  is the Faraday constant,  $k_B$  is the Boltzmann constant, and  $\phi_l$  is the electrolyte potential. The first and second terms on the right-hand side of the equation represent diffusion driven by the concentration gradient and migration induced by the electric field, respectively.

#### 2.7.2. Electrochemistry

The electrochemical behavior was simulated using the secondary current distribution method, which accounts for concentration gradients and electrode kinetics. Charge transport in the electrolyte is modeled using Ohm's law, given here as Eq. (4):

$$i_l = -\sigma_l \nabla \phi_l \quad (4)$$

where  $i_l$  is the current density vector and  $\sigma_l$  is the electrical conductivity of the electrolyte. The continuity of current density is enforced by Eq. (5):

$$\nabla \bullet i_l = 0 \quad (5)$$

To ensure periodic boundary conditions, a zero electric flux condition was applied to the lateral boundaries by using Eq. (6):

$$-n \bullet i_l = 0 \quad (6)$$

where  $n$  is the normal vector to the boundary. The local current density and overpotential of the electrode were modeled using the concentration-dependent kinetics described by the Butler-Volmer equation, given here as Eq. (7):

$$i_{\text{loc}} = i_o [c_R \exp\left(\frac{\alpha_a F \eta}{RT}\right) - c_O \exp\left(\frac{\alpha_c F \eta}{RT}\right)] \quad (7)$$

where  $i_{\text{loc}}$  is the local charge transfer current density,  $i_o$  is the overall exchange current density,  $c_R$  and  $c_O$  are the concentration of reduced and oxidized species, respectively,  $\eta$  is the overpotential,  $R$  is the gas constant, and  $\alpha_a$  and  $\alpha_c$  are the respective anodic and cathodic charge transfer coefficients. The detailed simulation parameters used in the modeling are presented in Table 1.

## 3. Results and discussion

The procedure used to fabricate LG via solid-state exfoliation under Ar or ambient conditions is shown schematically in Fig. 1a. Here, the vertical and shear stresses induced during the solid-state exfoliation process respectively lead to reductions in the particle size and number of stacked graphite layers [34]. Moreover, the PSA results in Fig. 1b and e demonstrate that the final graphite particle size is influenced by the specific atmosphere within the container. Thus, during solid-state exfoliation under an air atmosphere (Fig. 1b), the average graphite

**Table 1**

The parameters and their values used in the simulation model.

Classification	Description	Value [units]
Global	Molar mass of Li	6.941[g mol <sup>-1</sup> ]
	Density of Li	534 [kg m <sup>-3</sup> ]
	Initial concentration of Li	1000 [mol m <sup>-3</sup> ]
Flow	Li diffusivity of defect-free graphene	$7.95 \times 10^{-9}$ [cm <sup>2</sup> s <sup>-1</sup> ]
	Li diffusivity of defect-rich graphene	$1.49 \times 10^{-8}$ [cm <sup>2</sup> s <sup>-1</sup> ]
Electrostatic	Porosity of defect-free graphene	0.508
	Porosity of defect-rich graphene	0.446
	Exchange current density	10 [A m <sup>-2</sup> ]
Electrostatic	Relative equilibrium potential	0 [V]
	External potential on electrode	0.1 [V]
	Symmetry factor	0.5
	Net charge	1
	Electrical conductivity of electrolyte	0.81 [S m <sup>-1</sup> ]
	Activated specific surface area of defect-free graphene	$1.07 \times 10^7$ [1 m <sup>-1</sup> ]
	Activated specific surface area of defect-rich graphene	$7.99 \times 10^8$ [1 m <sup>-1</sup> ]

particle size gradually decreases from  $\sim 18 \mu\text{m}$  to  $\sim 9 \mu\text{m}$  within the first 5 days, and shows little change thereafter. Meanwhile, a decrease in the peak width indicates a narrower particle size distribution. By contrast, solid-state exfoliation under an Ar atmosphere (Fig. 1e) leads to a continuous decrease in the particle size to reach  $\sim 5 \mu\text{m}$  on day 8. Furthermore, from day 6 of the exfoliation process, particles smaller than  $1 \mu\text{m}$  begin to appear, thereby generating a bimodal distribution.

The full XRD pattern of the graphite sample is presented in Fig. S1 of the Supplementary Information. Here, both samples exhibit peaks corresponding to the hexagonal structure of graphite in the xy-plane and stacking along the c-axis, with notable peaks observed at  $2\theta = 26^\circ$ ,  $42^\circ$ , and  $45^\circ$  corresponding to the (002), (100), and (101) planes [34]. For further analysis, the changes in the (002) XRD peak during solid-state exfoliation under air and Ar atmospheres are shown in Fig. 1c and f, respectively. Thus, when solid-state exfoliation is performed under an air atmosphere (Fig. 1c), no significant peak broadening or increase in noise is observed as the solid-state exfoliation time increases. By contrast, the (002) XRD peak obtained during solid-state exfoliation under an Ar atmosphere exhibits broadening and an increase in noise with the increase in solid-state exfoliation time. This can be attributed to the reduction in crystalline size and increase in the proportion of exfoliated graphene due to the mechanical impacts exerted on graphite during the solid-state exfoliation process. Based on the full width at half maximum (FWHM) of the corresponding XRD peaks, the Scherrer equation [35] was used to calculate the crystalline sizes of the RGr and LG samples after 8 days of solid-state exfoliation (Table S1) [36]. Thus, the crystalline size of the initial graphite is 24.2 nm, while that of the RGr is slightly reduced to 18.5 nm, and that of the LG is significantly reduced to 9.5 nm.

The structures of the samples obtained via solid-state exfoliation under air and Ar atmospheres are further elucidated by the corresponding time-dependent Raman spectra in Fig. 1d and g, respectively. In each case, the G peak, which is commonly found in graphitic materials, is observed at  $1580 \text{ cm}^{-1}$ , while the D peak, which originates from

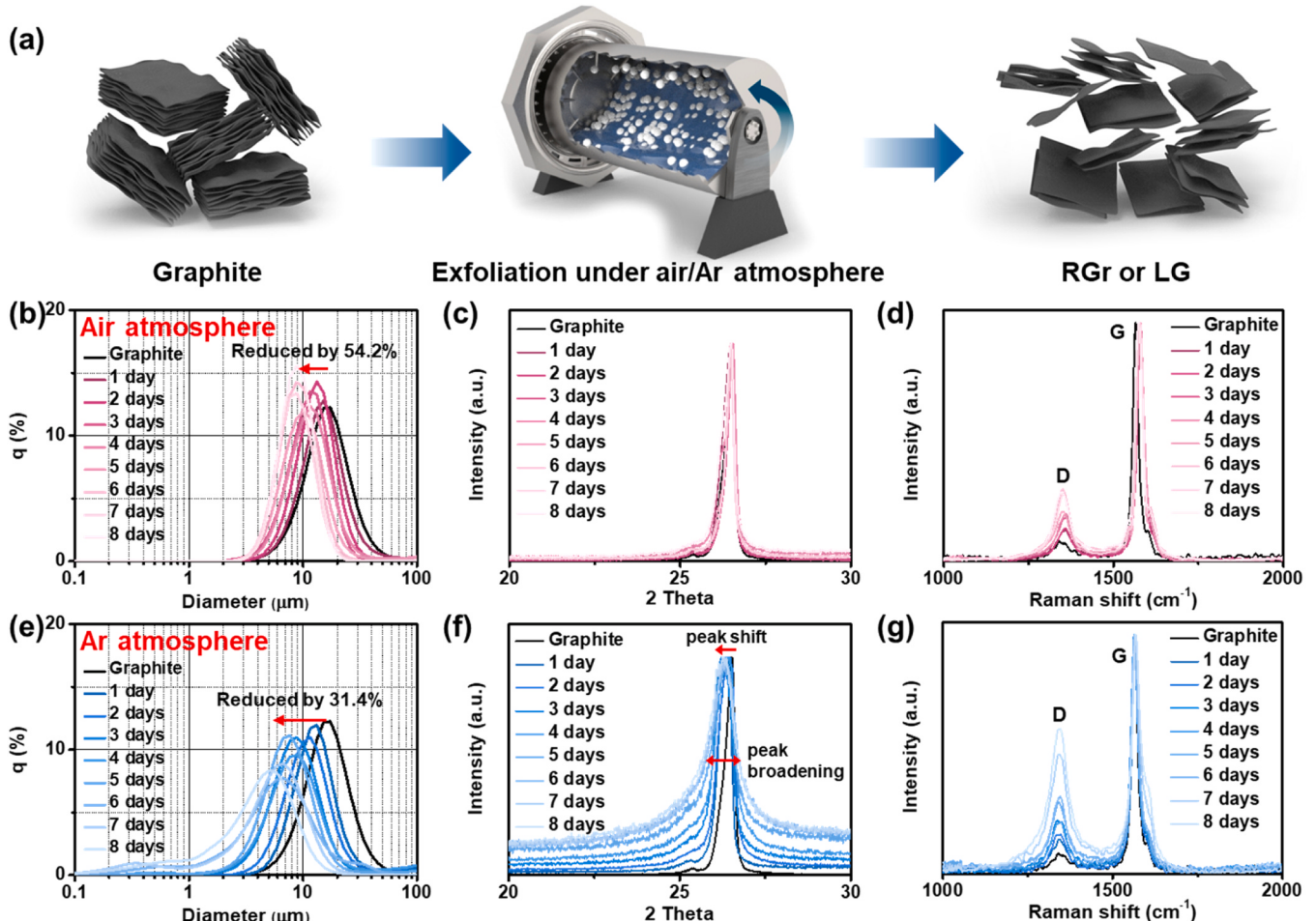


**Fig. 1.** (a) A schematic illustration of the solid-state exfoliation process. The time-dependent PSA distributions (b and e), (002) XRD peaks (c and f), and Raman spectra (d and g) of the graphite during solid-state exfoliation under (b–d) an air atmosphere and (e–g) an Ar atmosphere.

defects in the hexagonal structure of graphite, appears at  $1315\text{ cm}^{-1}$  [37]. When solid-state exfoliation is performed under air atmosphere (Fig. 1d), the intensity of the D peak increases during the first 5 days and shows no further increase thereafter. In addition, the D/G ratio is seen to increase from 0.083 for the graphite to 0.301 for the RGr on day 8. By comparison, when solid-state exfoliation is performed under an Ar atmosphere, the D peak exhibits a continuous increase in intensity throughout the entire process. Meanwhile, an increase in the D/G ratio from 0.083 to 0.606 indicates a significant increase in the number of defects in the hexagonal carbon structure of graphite under the Ar atmosphere. Taken together, these results indicate that graphite undergoes more effective pulverization during solid-state exfoliation under an Ar atmosphere compared to air.

The morphologies of the graphite, RGr and LG samples obtained after solid-state exfoliation under air and Ar atmospheres for 8 days are revealed by the SEM images in Fig. 2a–c. Here, the graphite (Fig. 2a)

exhibits particles with a size greater than  $5\text{ }\mu\text{m}$ , while voids are clearly observed between the flakes, thereby suggesting that the graphite powder contains an abundance of pores. After solid-state exfoliation under an air atmosphere, the RGr particles in Fig. 2b exhibit reductions in both the thickness and area of the planar structure. This can be attributed to the applied stress during exfoliation, which causes the particles to break down. Notably, much smaller particles are obtained after exfoliation under an Ar atmosphere (Fig. 2c). Moreover, as the particle size decreases, both the pore size and porosity are seen to decrease.

The transformation of the graphite into few-layered graphene due to solid-state exfoliation under an Ar atmosphere is clearly evidenced by the TEM analysis in Fig. 2d–f. Here, both the graphite (Fig. 2d) and the RGr (Fig. 2e) exhibit well-ordered c-axis layered structures indicative of multilayered graphene domains, whereas the LG (Fig. 2f) exhibits only a limited number of layers without any apparent long-range stacking

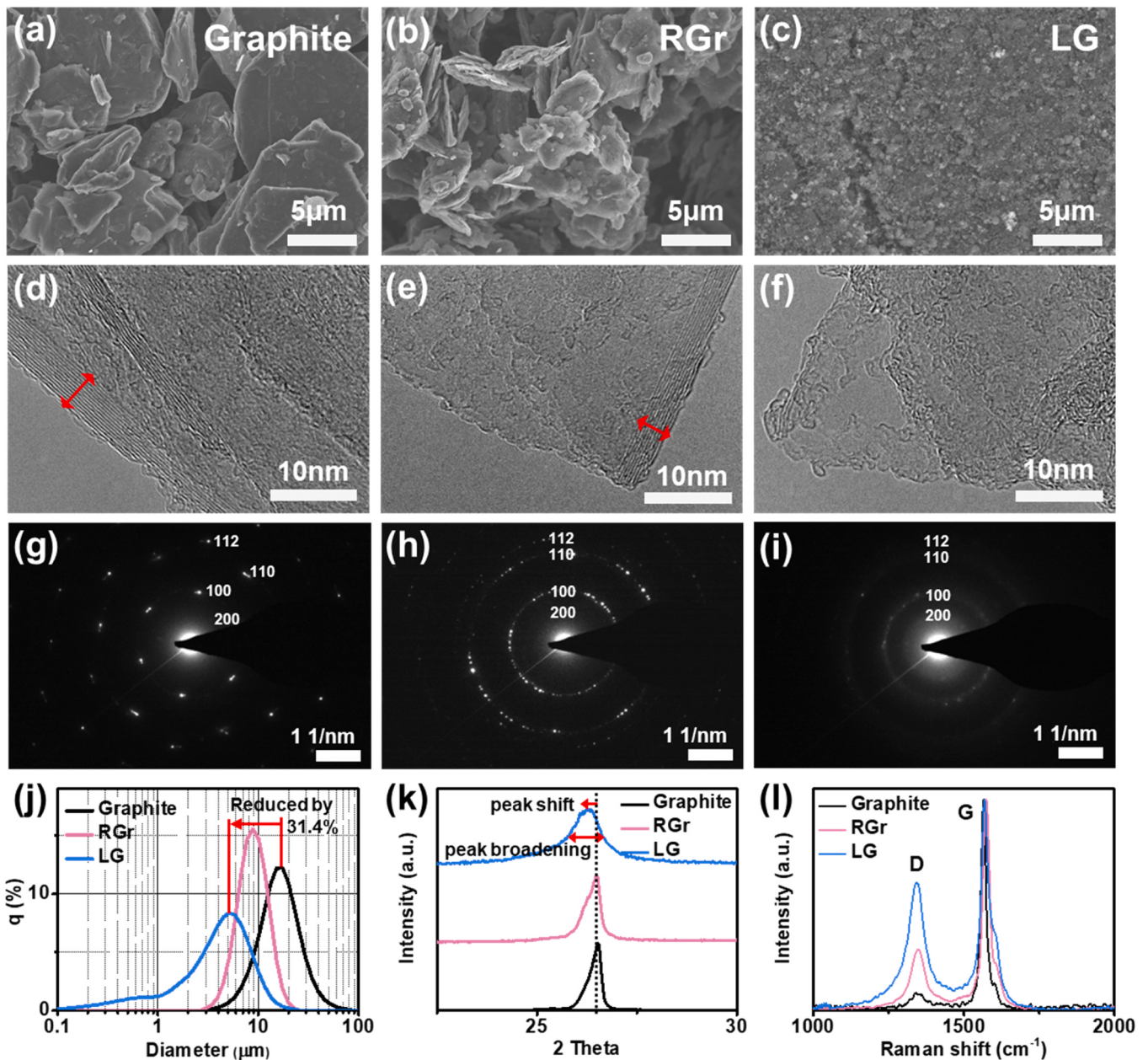


**Fig. 2.** The morphological and structural characteristics of the graphite samples before and after 8 days of solid-state exfoliation under air or Ar atmospheres. The SEM images, TEM images, and SAED patterns of (a, d, and g) the graphite, (b, e, and h) the RGr, and (c, f, and i) the LG. The comparative (j) PSA analyses, (k) (002) XRD patterns, and (l) Raman spectra of the three samples.

order. Furthermore, numerous defects induced by solid-state exfoliation damage are observed within the LG layers. More definitive evidence for the stacking and layered nature of the graphene structures in each sample is provided by the selected area electron diffraction (SAED) patterns in Fig. 2g–i. Here, all three samples exhibit characteristic SAED patterns corresponding to the typical graphitic (200), (100), (110), and (112) lattice planes [38]. However, while the graphite (Fig. 2g) exhibits a highly ordered diffraction pattern indicative of a single crystal, the RGr shows evident spot splitting, thereby indicating increased structural disorder and polycrystallinity. Moreover, in the case of the LG (Fig. 2i), the diffraction features are further degraded into faint rings, thereby suggesting a highly disordered stacking configuration. Overall, these structural variations reflect the atmosphere-dependent differences in the extent of fracture and defect formation during solid-state exfoliation, which in turn lead to various degrees of crystallinity loss and structural disorder in the resulting carbon materials. This is further evidenced by

the comparative PSA, XRD, and Raman analyses of the various samples before and after 8 days of solid-state exfoliation under air and Ar atmospheres in Fig. 2j–l. Thus, in the PSA results (Fig. 2j), the LG exhibits a smaller average particle size and a broader particle size distribution than the RGr. Notably, the LG exhibits a 31.4 % reduction in average particle size compared to that of the graphite. Meanwhile, the (002) XRD peak of the LG (Fig. 2k) shows a clear shift and noticeable broadening relative to that of the graphite, whereas that of the RGr remains relatively sharp and unshifted. Similarly, the Raman spectrum of the LG (Fig. 2l) exhibits a more significant increase in the D peak intensity than does the RGr, thereby indicating a higher degree of structural defects induced by solid-state exfoliation under an Ar atmosphere.

The fracture behaviors of the graphite under air or Ar atmospheres are examined in Fig. 3. First, the differences in the chemical bonding states of each sample are revealed by the O1s XPS peaks in Fig. 3a–c. Here, the graphite (Fig. 3a) exhibits a dominant peak at approximately

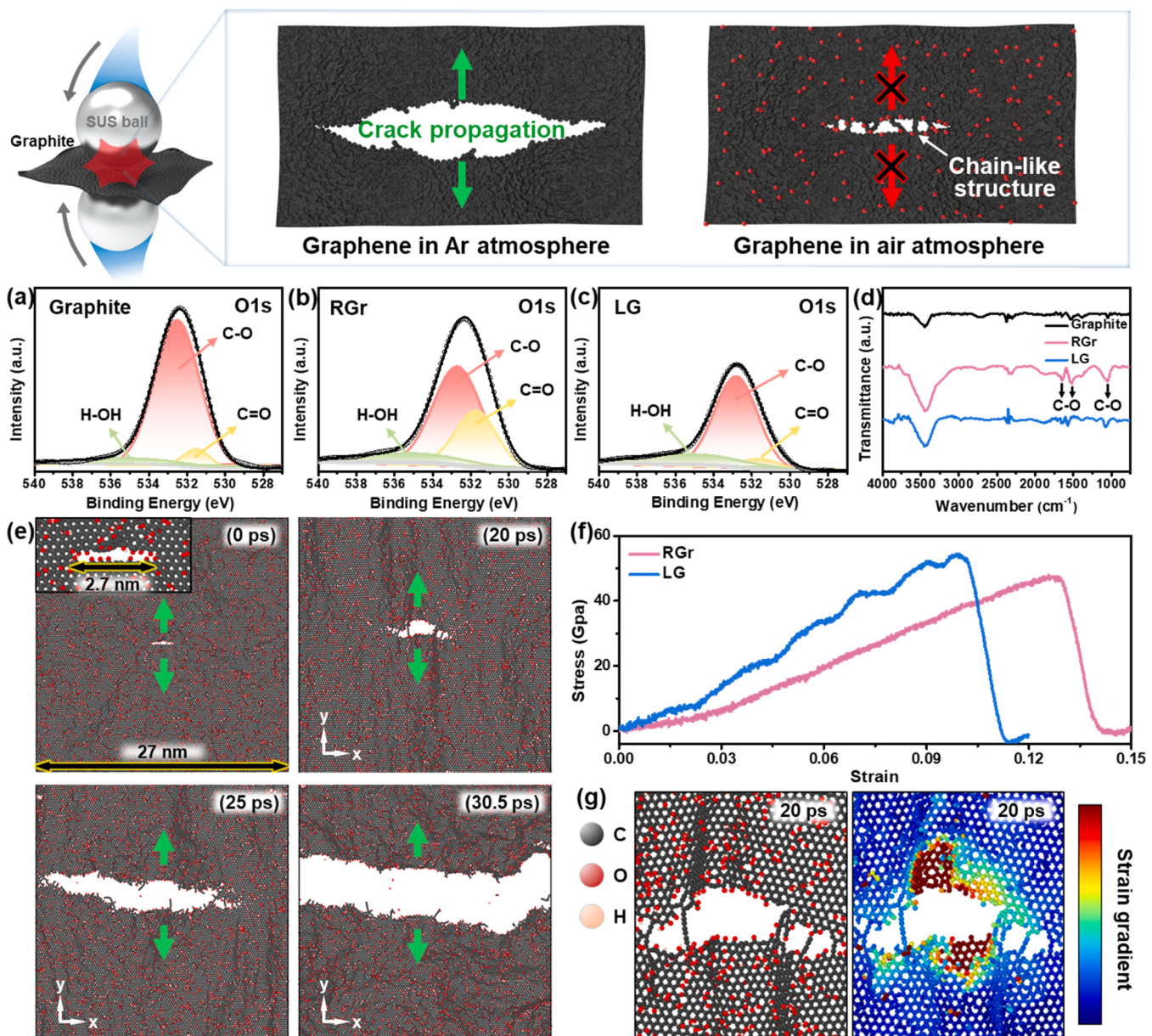


**Fig. 3.** (a–c) The XPS O1s spectra of (a) the graphite, (b) the RGr, and (c) the LG. (d) The comparative FT-IR spectra of the three samples. (e) The full fracture trajectories of the model graphite sheet under oxygen-poor (Ar) conditions, where the green arrow represents the strain direction. (f) The stress-strain curves of the model graphene sheets under oxygen-rich (RGr) and oxygen-poor (LG) conditions. (g) The fracture image (left) and strain gradient (right) of the graphene at 20 ps under oxygen-poor (Ar) conditions.

532.5 eV, which can be attributed to the presence of C–O bonds, along with additional peaks corresponding to C=O and H–OH bonds. By comparison, the RGr (Fig. 3b) exhibits a slight decrease in peak intensity, while the LG (Fig. 3c) exhibits a significant decrease. Based on the integrated areas of the O1s peaks, the ratio of oxygen-containing bonds in the graphite, RGr, and LG was calculated as 1.82:1.49:1. This indicates that the presence of oxygen in the exfoliation atmosphere significantly influences the extent of oxygen-containing surface bonds on the resulting sample. Furthermore, the relatively low intensity of the C=C peak in the C1s spectrum of LG suggests effective suppression of graphitic structure (Fig. S2). This is further demonstrated by the corresponding FT-IR spectra in Fig. 3d. Thus, in contrast to the graphite, the RGr exhibits distinct FT-IR peaks at around 1000, 1500 and 1700 cm<sup>-1</sup> due to the presence of C–O bonding. Although these C–O peaks are still present in the LG spectrum, its lower intensity compared to the RGr confirms a reduced amount of oxygen-containing functional groups. Furthermore, the corresponding EDS results Fig. S3 indicate oxygen contents of 3.50 and 2.01 wt% for the RGr and LG, respectively. This is consistent with the relative increase in the XPS O1s peak area of each sample, thereby further supporting the conclusion that the RGr has a higher oxygen content than the LG.

The fracture behaviors of graphite under the two different solid-state exfoliation conditions are further elucidated by molecular dynamics simulations. For this investigation, a graphene sheet containing a small central crack and functionalized with oxygen and hydroxyl groups was modeled, as shown in the upper left image of Fig. 3e. To enable a clear comparison of the fracture behavior, environments corresponding to  $\pm 10\%$  variation relative to standard air were assumed, thus resulting in functional group coverages of 10 % to represent Ar conditions and 35 % to represent oxygen-rich conditions. The relative ratio of these functional groups used in the simulation model was based on the above experimental XPS data, such that hydroxyl groups accounted for about 20 % while other oxygen-containing groups accounted for about 80 % (Table S2). Tensile strain was then applied along the y-direction until complete tearing occurred. The fracture trajectory for the simulated Ar atmosphere (i.e., oxygen-poor conditions) is visualized in Fig. 3e. The corresponding stress-strain curves in Fig. 3f clearly indicate that the graphite exhibits greater fracture toughness under oxygen-rich conditions than under oxygen-poor conditions. Moreover, the fracture images of the oxygen-poor case in Fig. 3g indicate that chain-like structures containing functionalized atoms are formed along the crack edges during deformation. Such structures have been suggested to contribute to improving the fracture toughness [39]. Indeed, these structures seem to exhibit a lower strain gradient compared to the crack center, potentially leading to resistance against crack propagation. This result suggests that the increased functionalization of graphene under oxygen-rich conditions promotes the formation of more chain-like structures during deformation, thereby enhancing the fracture toughness. These simulation results are consistent with the aforementioned experimental findings, where the particle sizes were approximately 5  $\mu\text{m}$  under Ar and 9  $\mu\text{m}$  under oxygen.

To examine how variations in particle size affect the packing density and uniformity of the coating layer, BET surface area and porosity measurements were performed for each material (Figs. S4a–c). Thus, the N<sub>2</sub> adsorption-desorption isotherms in Fig. S4a indicate specific surface areas of 4.75, 91.03, and 353.57 m<sup>2</sup> g<sup>-1</sup>, respectively. Furthermore, the BJH pore size distributions in Fig. S4b indicate that both the graphite and RGr samples have limited nanoscale porosity, which is likely due to their relatively large particle sizes and lower defect densities. By contrast, the LG exhibits a high density of nanopores with diameters below 10 nm. These findings suggest that the increased nanopore content in the LG originates from defect formation and void generation induced by the solid-state exfoliation process [40]. Moreover, the results in Fig. S4c indicate that the cumulative mercury intrusion volume per unit mass decreases in the order of RGr > graphite > LG, corresponding to porosities of 65.9 %, 50.8 %, and 44.6 %, respectively. The increased

porosity of the RGr relative to the graphite is likely due to the reduced packing density of the latter, which results from a narrower particle size distribution, as shown in Fig. 2j [41]. In the case of LG, the broadened and bimodal particle size distribution enhances the packing efficiency, thus leading to a lower porosity compared to both the graphite and the RGr [42]. This reduced porosity is advantageous for achieving a higher packing density during coating layer fabrication.

The effects of these material characteristics on the morphology of each coating layer are revealed by the SEM images in Figs. S4d–f. Here, the graphite@Cu (Fig. S4d) and RGr@Cu (Fig. S4e) exhibit non-uniform particle distributions and pronounced interparticle voids, which are attributable to their relatively large particle sizes. These structural inhomogeneities will directly compromise the density and uniformity of the coating layers. By contrast, the LG@Cu (Fig. S4f) displays a significantly more uniform particle distribution and markedly reduced void formation. This can be attributed to the combined effects of a smaller particle size and a broader, bimodal distribution, which together promote the formation of a dense and uniform coating.

The Li adsorption energy and Li storage mechanism of each material is investigated by DFT simulations and electrochemical measurements in Fig. 4. First, the effects of two types of defects, namely a Stone–Wales (SW) defect and a double-vacancy (DV) defect, on the Li adsorption behavior are revealed by the DFT results in Fig. 4a. Here, the adsorption sites are analyzed by focusing on hollow sites, which are known to be the most stable [43]. Thus, by using Eq. (1), the adsorption energies of the defect-less graphene, SW defected graphene, and DV defected graphene are calculated as -0.81, -1.74 and -2.36 eV, respectively. The more negative adsorption energies suggest that the introduction of defects into graphene promotes stronger interactions with Li, thus leading to lithophilic behavior. Indeed, the presence of defects, along with an increased fraction of edge sites, is known to enhance Li ion adsorption and contribute to Li storage kinetics via a pseudocapacitive effect [44]. Hence, the Li storage mechanisms of the graphite@Cu, RGr@Cu, and LG@Cu samples are further elucidated by the cyclic voltammetry (CV) measurements obtained at various scan rates in Fig. 4b–j. Thus, at a scan rate of 0.2 mV s<sup>-1</sup>, the graphite@Cu (Fig. 4b) exhibits a cathodic current of around 0.1 V and an anodic current of 0.3 V, which correspond to the respective intercalation and deintercalation of Li ions into and out of the layered structure of graphite. Notably, as the scan rate increases from 0.2 to 1.0 mV s<sup>-1</sup>, the area enclosed by the CV curve is increased, and the gap between the anodic and cathodic current peaks becomes wider, thereby indicating increased polarization. Similarly, the CV curve of the RGr@Cu (Fig. 4c) exhibits distinct peaks associated with Li intercalation, and shows increased polarization with the increase in scan rate. By contrast, the CV curve of the LG@Cu at a scan rate of 0.2 mV s<sup>-1</sup> (Fig. 4d) does not exhibit distinct intercalation-related peaks. This suggests that the graphene has been effectively exfoliated into extremely thin layers, thus resulting in a few-layered structure with limited capacity for Li intercalation. Furthermore, the presence of surface defects facilitates faster and more favorable Li adsorption on the LG. Despite increasing scan rates, the consistent gap between anodic and cathodic peaks indicates negligible polarization and suggests more reversible electrochemical behavior.

The charge storage mechanism can be elucidated by the power-law relationship in Eq. (8):

$$i = a \cdot v^b \quad (8)$$

where  $i$  is the peak current,  $v$  is the scan rate,  $a$  is a constant, and  $b$  is the exponent. This equation can be rearranged into a linear form by taking the logarithm of both sides, as shown in Eq. (9):

$$\log(i) = \log(a) + b \cdot \log(v) \quad (9)$$

where  $b$  is the slope. Here, a  $b$  value close to 0.5 indicates that the process is diffusion-controlled, whereas a  $b$  value close to 1.0 suggests that a capacitive mechanism dominates. As shown in Fig. 4e–g, the

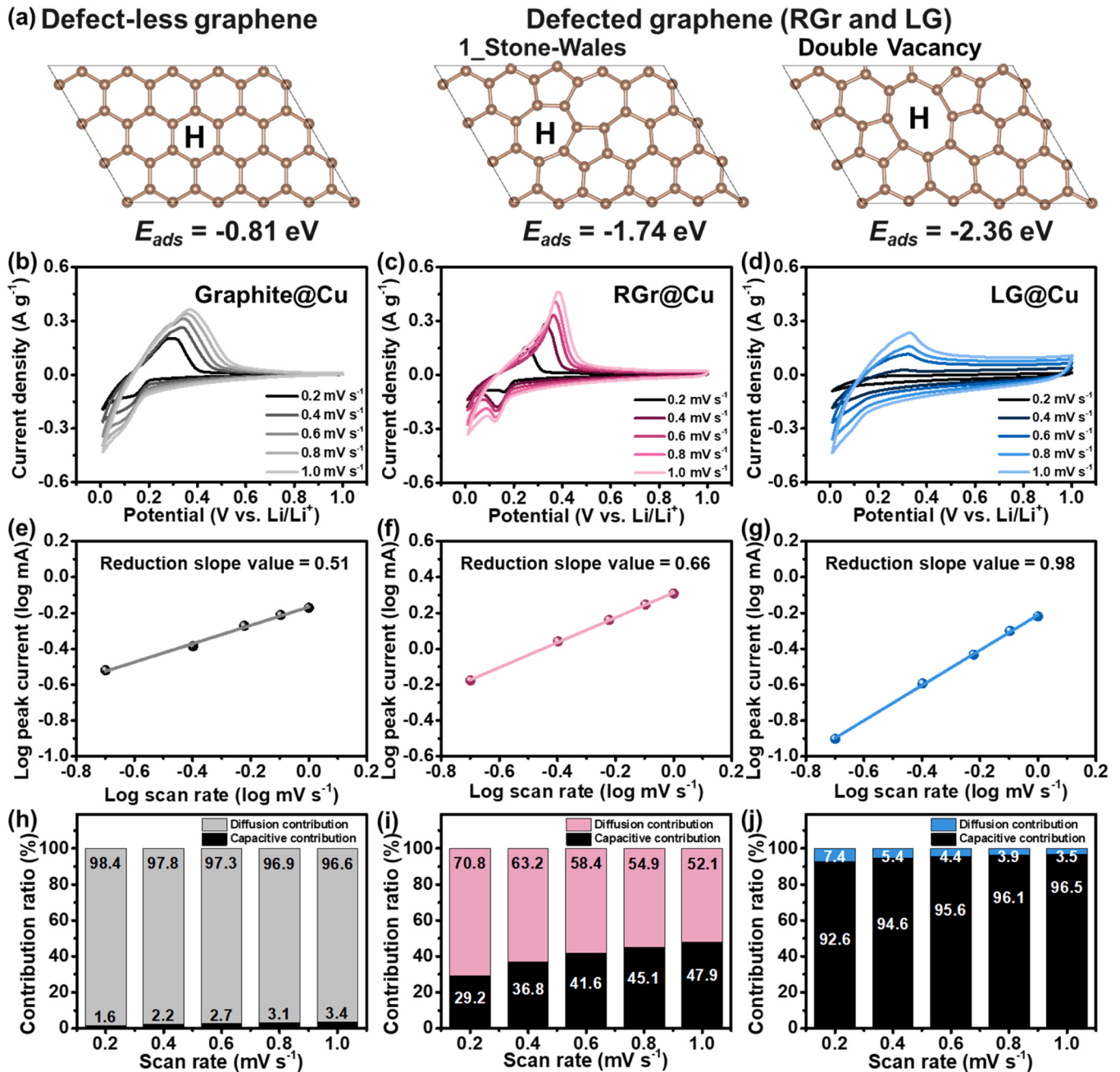


**Fig. 4.** (a) The Li adsorption energies for defect-less graphene, graphene with one SW defect and graphene with one DV defect, where H indicates a hollow site where Li can be adsorbed. (b-d) The CV curves, linear log(i)-log(v) plots and corresponding b-values, and relative capacitive and diffusion-controlled contributions to the total current at various scan rates for (b, e, and h) the graphite@Cu, (c, f, and i) the RGr@Cu, and (d, g, and j) the LG@Cu at various scan rates.

calculated  $b$  values for the reduction reactions of the graphite, RGr, and LG are 0.51, 0.66, and 0.98, respectively. Accordingly, the graphite exhibits predominantly diffusion-limited behavior during Li storage, while the RGr shows a mixture of diffusion-controlled and capacitive processes, and the LG is primarily governed by capacitive-dominated reactions. The relative contributions of diffusion-controlled and capacitive processes can be determined using Eq. (10):

$$i = k_1 v + k_2 v^{1/2} \quad (10)$$

where  $k_1$  represents the capacitive (surface-controlled) contribution, and  $k_2 v^{1/2}$  represents the diffusion-controlled contribution [45]. Based on this equation, the relative contributions of capacitive and diffusion-controlled processes to the overall Li storage behaviors of the

graphite@Cu, RGr@Cu, and LG@Cu are shown in Fig. 4h–j. Thus, at a scan rate of 0.2 mV s<sup>-1</sup>, the diffusion-controlled contribution in the graphite@Cu is 98.4 %, thereby indicating that the Li storage kinetics are predominantly governed by diffusion processes. As the scan rate is increased to 1.0 mV s<sup>-1</sup>, however, the diffusion contribution slightly decreases to 96.6 %, as the Li ions have insufficient time to diffuse into the bulk structure and instead participate in surface reactions. This results in an increased capacitive contribution and a corresponding decline in diffusion-controlled behavior. In the case of the RGr@Cu, the diffusion and capacitive contributions at 0.2 mV s<sup>-1</sup> are 70.8 % and 29.2 %, respectively, thereby indicating a mixed kinetic mechanism. As with the graphite@Cu, the diffusion contribution in the RGr@Cu decreases with the increase in scan rate, reaching 52.1 % at 1.0 mV s<sup>-1</sup>. By contrast, the LG@Cu exhibits distinctly capacitive-dominated behavior.

At  $0.2 \text{ mV s}^{-1}$ , the diffusion contribution is only 7.4 %, while the capacitive component reaches 92.6 %. This behavior is attributed to the limited layered structure and high density of defects in the LG, which facilitate  $\text{Li}^+$  adsorption and fast surface redox reactions, characteristic of pseudocapacitive storage [44,46]. These results further demonstrate the superior rate capability and high reversibility of the LG@Cu-based cell.

The differences in electrode reversibility observed in the half-cell tests are elucidated by the ionic conductivity and interfacial resistance measurements, Li plating simulations, and post-plating SEM images in

**Fig. 5.** First, the  $\text{Li}^+$  diffusion coefficient values of the graphite@Cu, RGr@Cu, and LG@Cu are determined from the corresponding GITT curves in Fig. 5a. Under identical y-axis scaling, these samples exhibit voltage (IR) drops of 63, 62, and 34 mV, respectively, with the LG@Cu exhibiting a markedly lower value. From these results, the ionic diffusion coefficient can be calculated based on Fick's second law, as described by Eq. (11):

$$D_{\text{Li}^+} = \frac{4}{\pi\tau} \left( \frac{m_b}{\rho S} \right)^2 \left( \frac{\Delta E_s}{\Delta E_t} \right)^2 \quad (11)$$

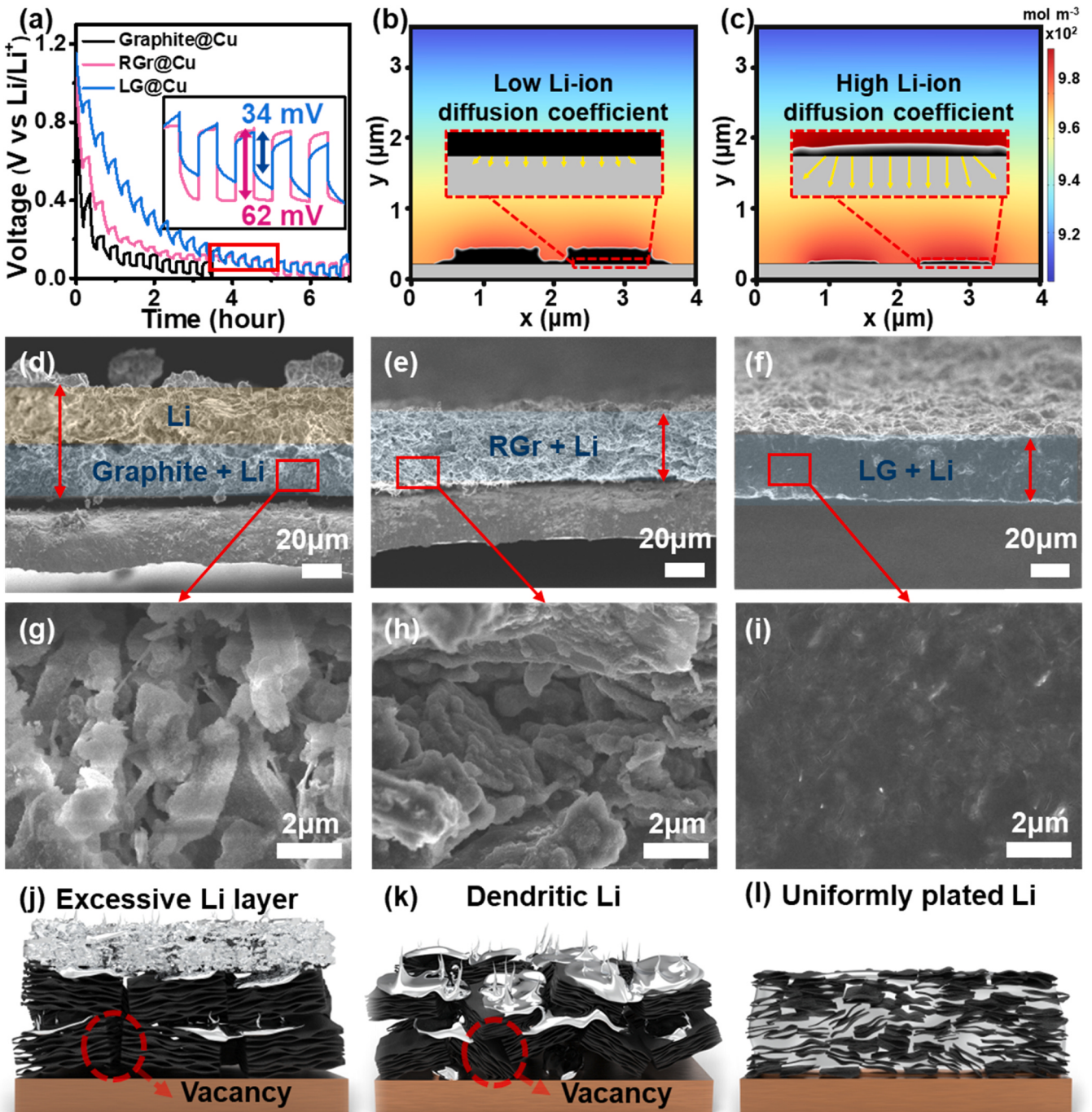


**Fig. 5.** (a) The GITT curves of Li cells containing the graphite@Cu, RGr@Cu, and LG@Cu samples. Color maps representing the distribution of Li-ion concentrations in (b) defect-free graphene and (c) defect-rich graphene (based on FEM simulations and GITT measurements), along with inset schematic diagrams showing the growth of Li dendrites (black) on graphene (gray), where the arrows indicate the magnitude of the Li-ion flux. Low-resolution cross-sectional SEM images of (d) the graphite@Cu, (e) the RGr@Cu, and (f) the LG@Cu after Li plating. The corresponding high-magnification SEM images of the regions indicated by the red rectangles. Schematic illustrations of the Li plating behavior on (j) the graphite@Cu, (k) the RGr@Cu, and (l) the LG@Cu.

where  $\tau$  denotes the duration of the current pulse,  $S$  is the area of the copper foil,  $\rho$  is the density of the active material,  $m_b$  is the molar mass of the host, and  $\Delta E_t$  and  $\Delta E_s$  are the respective steady-state voltage change and instantaneous voltage drop during each galvanostatic titration interval. The calculated average Li<sup>+</sup> diffusion coefficients for the graphite@Cu, RGr@Cu, and LG@Cu are  $7.95 \times 10^{-9}$ ,  $1.11 \times 10^{-8}$ , and  $1.49 \times 10^{-8} \text{ cm}^2 \text{ s}^{-1}$ , respectively.

The ionic transport and interfacial properties are further elucidated by the EIS results in Fig. S5, where the graphite@Cu, RGr@Cu, and LG@Cu half-cells exhibit ohmic resistances of 23.13, 6.72, and 2.95 Ω, respectively, along with charge-transfer resistances of 827.01, 393.04, and 197.51 Ω. The substantially lower ohmic resistance of the LG@Cu is attributed to its improved interfacial stability, arising from enhanced particle uniformity due to the smaller average LG particle size and broader size distribution [47,48]. Meanwhile, the reduced charge-transfer resistance of the LG@Cu is ascribed to the high surface defect density of the LG, which promotes Li<sup>+</sup> adsorption and facilitates electron transport at the interface [49].

The interfacial properties of the graphite@Cu, RGr@Cu, and LG@Cu samples are revealed by the contact angle measurements in Fig. S6. Thus, when equal volumes of deionized (DI) water (a polar solvent) are dropped onto each sample, the graphite@Cu and RGr@Cu exhibit contact angles of 108° and 39°, respectively, which are significantly larger than that of the LG@Cu (30°). The lower contact angle of the LG reflects superior electrolyte wettability, which promotes better infiltration into the material and increases the active surface area, thereby enhancing the electrochemical reaction kinetics [50]. The combination of low resistance, high ionic conductivity, and improved wettability of the LG, contributes to its superior reversible Li accommodation.

In the case of the SUS|SUS symmetric cells with graphite@PP, RGr@PP, and LG@PP separators, the EIS results in Fig. S7 indicate ohmic resistances of 1.56, 1.69, and 1.77 Ω, respectively. Based on these values, the ionic conductivity ( $\sigma$ ) of each separator-electrode system can be calculated by using Eq. (12):

$$\sigma = \frac{d}{R \cdot A} \quad (12)$$

where  $d$  is the sample thickness,  $R$  is the ohmic resistance, and  $A$  is the area of the separator. Thus, the ionic conductivities of the graphite@PP, RGr@PP, and LG@PP separators are calculated as  $1.18 \times 10^{-3}$ ,  $1.23 \times 10^{-3}$ , and  $1.33 \times 10^{-3} \text{ S cm}^{-1}$ , respectively, thereby indicating that the LG effectively enhances the ionic conductivity. Schematic comparison of the resistance and ion diffusion characteristics of the graphite, RGr, and LG during Li interaction is presented in Fig. S8. Thus, due to their larger particle sizes and extensive layer stacking, the graphite and RGr exhibit higher resistances and slower Li-ion transport characteristics. Conversely, the smaller particle size, fewer stacked layers, and abundant structural defects of the LG afford a lower diffusion resistance and facilitate more reversible interactions with Li.

The influence of material properties on Li transport is further elucidated by the FEM simulation results in Fig. 5b and c. Here, an asymmetric Li–Cu cell was modeled using the Li<sup>+</sup> diffusion coefficient values obtained from the abovementioned GITT measurements for defect-free and defect-rich graphene. In addition, the effects of specific surface area and porosity were incorporated to simulate how the structural features of graphene influence the Li transport behavior. The resulting color maps representing the distribution of Li-ion concentrations in each sample are presented here, along with inset schematic diagrams showing the growth of Li dendrites (black) on graphene (gray), where the arrows indicate the magnitude of the Li-ion flux. Thus, the low surface area and poor diffusivity of the defect-free graphene leads to localized dendrite formation due to limited Li-ion diffusion into the bulk (Fig. 5b), whereas the higher surface area and diffusion coefficient of the defect-rich graphene enables more uniform Li-ion flux into the material, thereby mitigating dendritic growth (Fig. 5c). These results highlight the critical

roles of surface defects and specific surface area in enhancing Li accommodation and suppressing dendrite formation by improving Li transport.

It has been reported that carbon-based materials such as graphene can develop lithiophilic characteristics after uniform lithiation, which in turn promotes homogeneous Li plating [21–23]. To experimentally verify whether the abovementioned differences in Li accommodation characteristics translate into improved Li plating behavior, graphite@Cu, RGr@Cu, and LG@Cu samples were subjected to Li plating at an areal current density of  $2 \text{ mA cm}^{-2}$  and an areal capacity of  $1 \text{ mAh cm}^{-2}$ . The cells were subsequently disassembled for cross-sectional SEM analysis, as shown in Fig. 5d–i. Here, the formation of an additional Li layer is clearly observed on top of the graphite@Cu coating (Fig. 5d), thereby suggesting that the sluggish Li<sup>+</sup> diffusion leads to surface accumulation and irreversible Li deposition. Moreover, the corresponding high-magnification SEM image in Fig. 5g confirms the presence of dendritic Li structures and voids within the coating. In the case of the RGr@Cu (Fig. 5e), however, the smaller particle size enables faster Li uptake and lower resistance, thereby preventing the formation of an additional Li layer. Nevertheless, the high-magnification image in Fig. 5h still reveals the presence of dendritic Li and a porous Li morphology, thereby indicating limited ability to buffer against volume changes during plating/stripping. The formation of dendritic Li structures induces the accumulation of inactive Li over repeated cycles, resulting in decreased CE and overall cell degradation [51]. By contrast, the LG@Cu exhibits uniform and dense Li deposition without the formation of an additional Li layer (Fig. 5f). In this case, the high-magnification SEM image reveals a dendrite-free Li layer with minimal voids (Fig. 5i). Based on these images, the thicknesses of the deposited Li layers were approximately 58.0, 34.8, and 32.2  $\mu\text{m}$  for graphite@Cu, RGr@Cu, and LG@Cu, respectively. These results suggest that employing LG as the current collector enables the most compact Li deposition with minimal volumetric expansion, thereby promoting the most stable cell operation. This improved behavior is attributed to the small particle size, low resistance, and abundant structural defects of LG, which collectively enable rapid and uniform Li accommodation. Moreover, the lithiophilic nature of LG promotes homogeneous Li nucleation and plating across the surface, thereby effectively accommodating the volume changes associated with Li metal anodes. The layers and structures formed on each sample are shown schematically in Fig. 5j–l.

The applicability of each material as a current collector in an Li–Cu half-cell is demonstrated by the electrochemical measurements in Fig. 6. Thus, under a current density of  $1 \text{ mA cm}^{-2}$  and an areal capacity of  $1 \text{ mAh cm}^{-2}$ , the Li–Cu cells exhibit comparable initial CE values of approximately 90 % (Fig. 6a). During multiple repeat cycles, however, the CE values of the cells containing the graphite@Cu and RGr@Cu current collectors are seen to decline progressively, eventually reaching about 60 % by the 120th cycle, thereby indicating degradation in electrochemical performance. By contrast, the cell containing the LG@Cu current collector maintains a high CE of 89.9 % even after 120 cycles. For further analysis, the voltage profiles obtained during the first cycle are shown in Fig. 6b. Here, the cell containing the pure Cu current collector exhibits an abrupt drop in voltage to below 0 V, which suggests immediate Li plating onto the Cu foil. For the cell containing the graphite@Cu current collector, however, the voltage gradually decreases from approximately 0.2 V to reach 0 V at an areal capacity of around  $0.5 \text{ mAh cm}^{-2}$ . This behavior suggests that Li does not plate directly onto the graphite surface but instead intercalates into its layered structure. By contrast, the cell containing the RGr@Cu (with fewer graphene layers than the graphite@Cu) shows a reduced extent of Li intercalation, such that the voltage reaches 0 V at an areal capacity of approximately  $0.3 \text{ mAh cm}^{-2}$ . Moreover, for the cell containing the LG@Cu, which lacks a significant interlayer structure, lithiation is limited to approximately  $0.1 \text{ mAh cm}^{-2}$ . In the 50th and 100th cycles, however, the cells containing the graphite@Cu and RGr@Cu each exhibit an immediate voltage drop to below 0 V (Fig. 6c and d). These

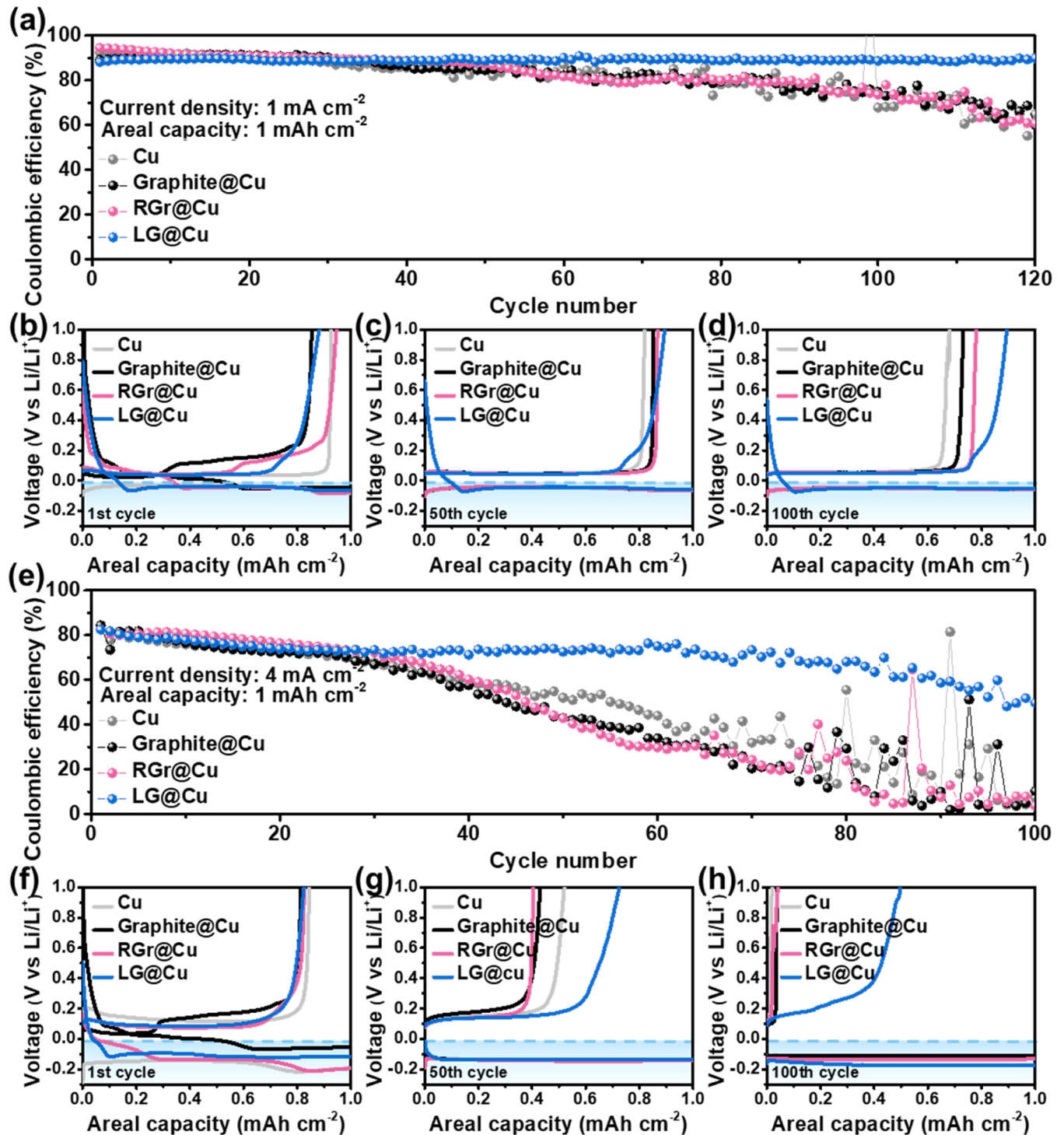


**Fig. 6.** The electrochemical performance of Li–Cu cells containing Cu, graphite@Cu, RGr@Cu, and LG@Cu current collectors: (a) the cycling performance at a current density of  $1 \text{ mA cm}^{-2}$  and an areal capacity of  $1 \text{ mAh cm}^{-2}$ ; the corresponding voltage profiles during (b) the 1st, (c) the 50th, and (d) the 100th cycles; (e) the cycling performance at a higher current density of  $4 \text{ mA cm}^{-2}$  with an areal capacity of  $1 \text{ mAh cm}^{-2}$ ; the corresponding voltage profiles during (f) the 1st, (g) the 50th, and (h) the 100th cycles.

results indicate that repeated Li plating and stripping induce irreversible capacity loss in graphite, thereby hindering further lithiation and leading to immediate Li plating [52]. This degradation promotes the growth of Li dendrites and the formation of dead Li, thus resulting in a gradual decline in CE over repeated cycling. By contrast, the voltage profiles of the LG@Cu cell during the 50th and 100th cycles closely resemble that obtained in the first cycle, thereby indicating stable reversibility throughout long-term cycling.

Under high-rate conditions (current density =  $4 \text{ mA cm}^{-2}$ ) the various cells exhibit comparable initial CEs of  $\sim 80\%$  (Fig. 6e). However, the CEs of the graphite@Cu and RGr@Cu cells begin to decline after 30 cycles, and have dropped to below 30 % after the 70th cycle, thereby suggesting the onset of internal short circuits. By contrast, the LG@Cu cell maintains a relatively high CE of 49.8 % even after 100 cycles, thus confirming its superior cycling stability. In the initial charge-discharge curves (Fig. 6f), the LG@Cu cell exhibits the smallest

lithiation plateau, which is consistent with earlier observations. Moreover, the charge-discharge curve of this cell largely maintains its shape even during the 50th and 100th cycles (Fig. 6g and h), thus further supporting the stable and reversible behavior of LG-based electrodes over extended cycling.

The practical applicability of each material as a current collector in an anode-less full cell with an LFP cathode is evaluated within a voltage window of 2.5–4.0 V in Fig. 7. At 0.5 C (Fig. 7a), the cell containing the LG@Cu current collector delivers a superior initial capacity of 157.4 mAh g<sup>-1</sup>, compared to 150.0 and 151.1 mAh g<sup>-1</sup> for the cells containing graphite@Cu and RGr@Cu, respectively. This is attributed to uniform deposition of Li on the LG surface during the initial cycles, in contrast to the inhomogeneous and irreversible plating of dendritic Li on the graphite@Cu and RGr@Cu surfaces due to non-uniform Li accommodation. Consequently, as cycling progresses, the graphite@Cu- and RGr@Cu-based cells each exhibit rapid and continuous capacity fading, such that the capacity eventually drops to approximately 40 mAh g<sup>-1</sup> at around the 40th cycle, while the LG@Cu-based cell maintains a capacity of 155.7 mAh g<sup>-1</sup> even after 100 cycles. This indicates that LG@Cu not only accommodates Li uniformly during the initial cycle, but also enables stable Li plating and stripping over prolonged cycling, thereby contributing to reversible capacity retention.

In the initial galvanostatic voltage profiles (Fig. 7b), the charging plateau at around 3.5 V corresponds to the extraction of Li-ion from the LFP cathode and its subsequent plating onto the current collector. Meanwhile, the discharging plateau at around 3.4 V represents the stripping of Li from the current collector and its reinsertion into the FePO<sub>4</sub> cathode, thereby reforming LFP. The polarization gaps in these voltage profiles at specific capacities of 72.5 mAh g<sup>-1</sup> are compared in Fig. 7c. Here, the cells containing the graphite@Cu and RGr@Cu exhibit polarization gaps of 208 and 198 mV, respectively, compared to only 93 mV for the cell containing the LG@Cu. This indicates that the lower Li plating/stripping overpotential of the LG@Cu originates from its abovementioned characteristics, including its high Li-ion diffusion coefficient, low charge transfer resistance, and large surface area, which

facilitate a more uniform current distribution during operation.

The high rate performances of the various cells are elucidated by the electrochemical test results at 1 C in Fig. 7d-f. Consistently with the above results, the LG@Cu-based cell exhibits the highest initial capacity, at 147.5 mAh g<sup>-1</sup>, compared to 136.1 and 143.5 mAh g<sup>-1</sup> for the graphite@Cu and RGr@Cu, respectively (Fig. 7d). After 100 cycles, the cells containing the graphite@Cu and RGr@Cu exhibit negligible capacity values, while that containing the LG@Cu retains a capacity of 130.8 mAh g<sup>-1</sup>, thereby demonstrating its excellent cycling retention. Moreover, the voltage profiles obtained during the first cycle at 1 C (Fig. 7e) indicate a larger polarization gap than that observed at 0.5 C (Fig. 7b). Specifically, the polarization gaps of the graphite@Cu, RGr@Cu, and LG@Cu cells at 1 C are 337, 274, and 178 mV, respectively (Fig. 7f), thereby confirming that LG@Cu consistently exhibits the lowest overpotential. Taken together, these results highlight the effectiveness of the LG@Cu current collector in enabling stable and low-resistance Li plating even under high-rate conditions.

To further evaluate the feasibility of implementing LG in next-generation energy storage systems, Li-S full cells were assembled and tested within the voltage window of 1.7–2.8 V, as illustrated in Fig. 8. In such Li-S batteries, carbon-based materials are commonly employed as separator coatings due to their ability to adsorb Li polysulfides, thereby suppressing their diffusion and mitigating the shuttle effect. In addition, a dense carbon layer can function as a physical barrier to further restrict polysulfide migration. To evaluate these mechanisms, the cycling performance of the PP, graphite@PP, RGr@PP, and LG@PP cells at 0.2 C are compared in Fig. 8a, while the corresponding galvanostatic charge-discharge profiles during the 1st and 100th cycles are presented in Fig. 8b and c, respectively. Here, the discharge plateau at around 2.3 V corresponds to the reduction of elemental sulfur (S<sub>8</sub>) into soluble Li polysulfides (Li<sub>2</sub>S<sub>x</sub>, 4 ≤ x ≤ 8), while that at around 2.1 V reflects their subsequent conversion into insoluble Li<sub>2</sub>S or Li<sub>2</sub>S<sub>2</sub> (1 ≤ x ≤ 2). During the initial cycle, the graphite@PP cell exhibits a discharge capacity of 1029.2 mAh g<sup>-1</sup> compared to 900.5 mAh g<sup>-1</sup> for the pristine PP separator, thereby indicating that the carbon layer enhances the

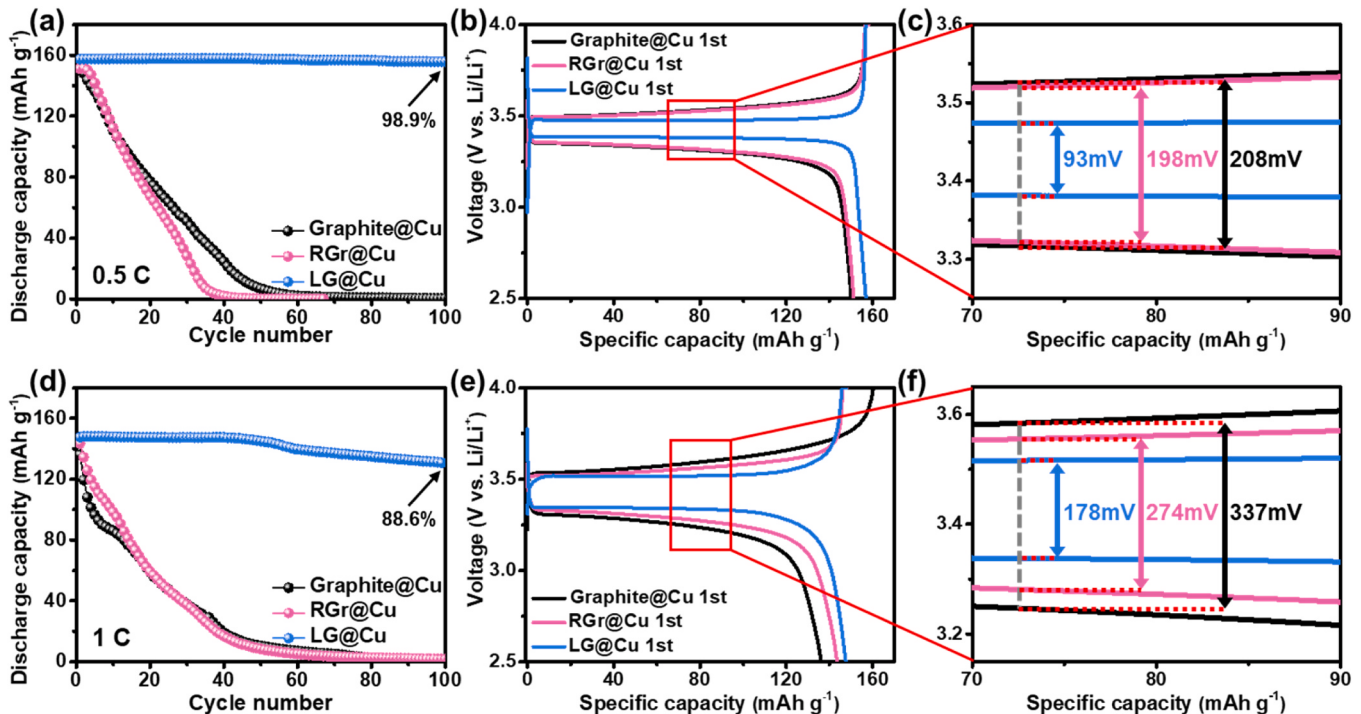


**Fig. 7.** The comparative performance characteristics of the various materials as current collectors in anode-less LFP cells. (a) The capacity retention during 100 cycles at 0.5 C. (b) The voltage profiles during the 1st cycle. (c) A comparison of the polarization gaps during the first cycle. (d) The capacity retention during 100 cycles at 1 C. (e) The corresponding voltage profiles during the 1st cycle at 1 C. (f) A comparison of the polarization gaps at 1 C.

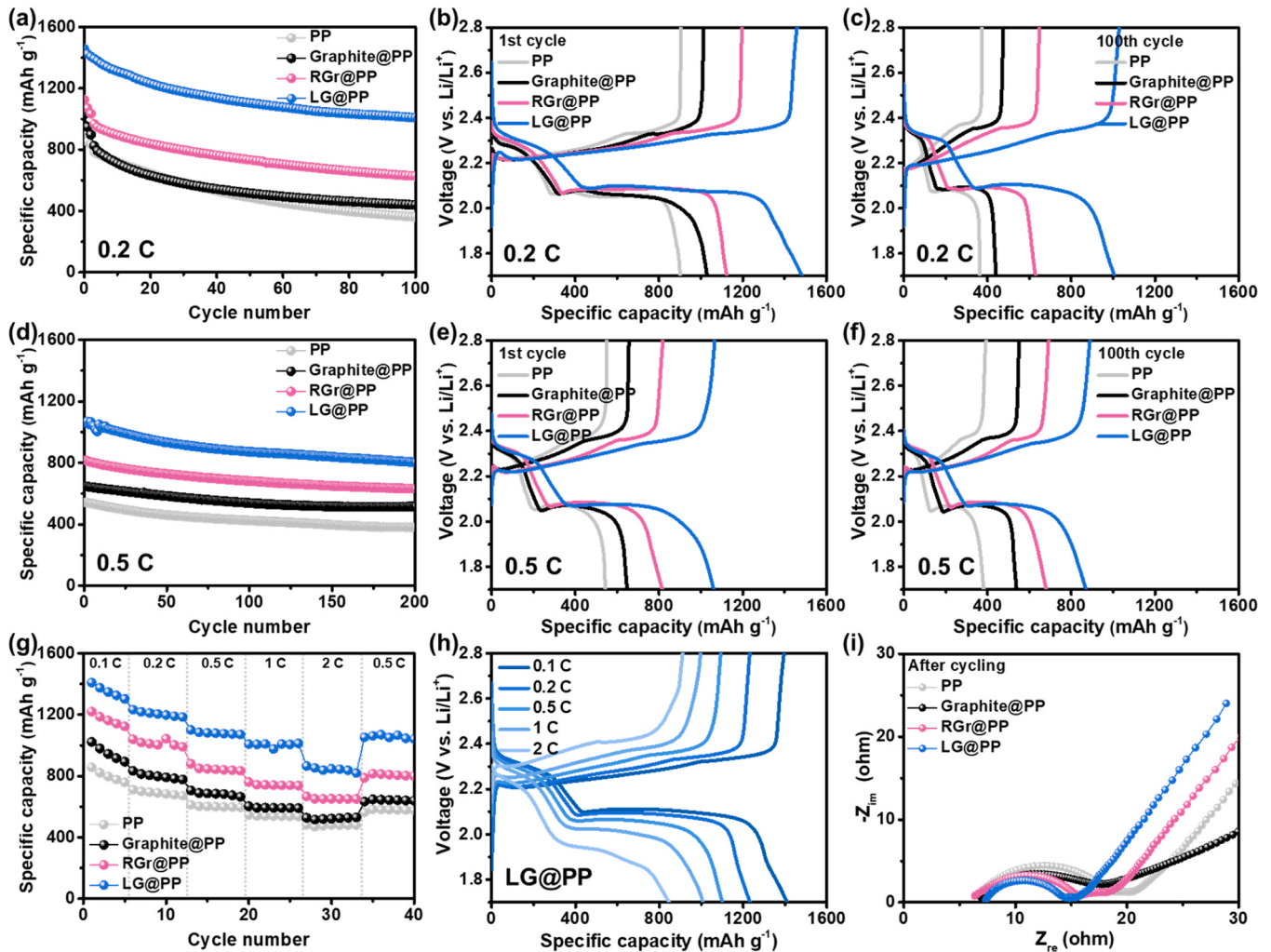


**Fig. 8.** The electrochemical performances of the various Li-S full cells. (a) The capacity retention during 100 cycles at 0.2 C. The corresponding charge–discharge voltage profiles during (b) the 1st and (c) 100th cycles. (d) The capacity retention during 200 cycles at 0.5 C. The corresponding charge–discharge voltage profiles during the (e) 1st and (f) 100th cycles. (g) The comparative rate capabilities at 0.1–2 C. (h) The charge–discharge voltage profiles of the LG@PP cell at each current rate. (i) The post-cycling EIS spectra of the various cells.

performance by adsorbing and physically blocking soluble polysulfides. By the 100th cycle, however, the capacity of the PP cell has declined to 363.1 mAh g<sup>-1</sup> due to polysulfide dissolution, while that of the graphite@PP cell remains at 440.1 mAh g<sup>-1</sup>, being limited by irreversible Li layer formation. Meanwhile, the capacity of the RGr@PP cell has decreased from its initial value of 1124.0 mAh g<sup>-1</sup> to 629.0 mAh g<sup>-1</sup>, which is likely due to degradation of the RGr coating. By contrast, the LG@PP cell delivers an exceptionally high initial capacity of 1484.3 mAh g<sup>-1</sup>, which can be attributed to the effective adsorption of polysulfides by the defect-rich and dense LG layer [53–56]. Moreover, this cell maintains a capacity of 1005.0 mAh g<sup>-1</sup> even after 100 cycles, with no significant interfacial degradation or additional Li accumulation.

The corresponding results at a higher current density of 0.5 C are presented in Fig. 8d–f, where the LG@PP cell continues to exhibit a superior performance due to sustained suppression of polysulfide migration. Thus, during the first cycle, the discharge capacities of the PP, graphite@PP, RGr@PP, and LG@PP cells are 543.8, 647.6, 813.8, and 1060.3 mAh g<sup>-1</sup>, respectively. Moreover, a similar overall trend is observed, with reduced capacities of 381.5, 537.4, 679.1, and 871.2 mAh g<sup>-1</sup>, respectively, after 200 cycles.

The enhanced ionic conductivity and interfacial stability of the LG@PP-based cell compared to the other cells are further elucidated by the comparative rate capability measurements at 0.1–2 C in Fig. 8g.

Here, the LG@PP cell consistently delivers the highest capacity across all current rates, thereby indicating high reversibility and efficient charge transport. The voltage profiles of each cell exhibit stable shapes without any noticeable side reactions (Fig. 8 h and S8). Moreover, the interfacial degradation and charge transfer resistance characteristics are revealed by the post-cycling EIS measurements in Fig. 8i. Here, the charge transfer resistances values of the PP, graphite@PP, RGr@PP, and LG@PP cells are found to be 12.5, 10.6, 9.4, and 7.2 Ω, respectively, thereby suggesting that the LG@PP cell provides the most efficient charge transfer. This is likely due to minimal interfacial degradation and enhanced electrochemical reversibility [57,58].

#### 4. Conclusions

This study elucidated the fracture behavior of graphite under different solid-state exfoliation atmospheres and clarified how differences in the macro-/micro-structure lead to performance variations in lithium metal batteries (LMBs). During solid-state exfoliation under an air atmosphere, oxygen-containing functional groups on the graphite surface suppress the propagation of microcracks, thereby reducing the exfoliation efficiency. By contrast, under an Ar atmosphere, the absence of oxygen-containing functional groups enables more efficient graphite exfoliation and particle size reduction, while a greater number of

lithiophilic atomic defects are observed on the graphene surface. Furthermore, the fracture behavior of graphene under different atmospheres and the Li-ion adsorption energies at defect sites were further verified by molecular dynamics (MD) simulations and density functional theory (DFT) calculations, respectively. The few-layered graphene structure and small particle size of lithiophilic graphene (LG) contributed to a high Li-ion diffusion coefficient and low resistance. Moreover, the abundant defects on the graphene surface promoted pseudocapacitive-dominated lithiation, a kinetically favorable process that ultimately leads to more uniform Li plating. Due to these advantages, the cells employing LG-coated copper (LG@Cu) in both half-cell and anode-less full cell configurations exhibited significantly improved long-term cycling performance and capacity compared to those using graphite@Cu and RGr@Cu. When used as a separator in an Li–S cell, the abundant defects in LG enhanced the adsorption of Li polysulfides, while its broad size distribution contributed to the formation of a uniform and compact coating layer, which further suppressed polysulfide diffusion to afford the maximum capacity. This study not only provides mechanistic insights into graphite fracture under different exfoliation atmospheres but also introduces LG as a versatile and scalable material for advanced energy storage systems.

#### CRediT authorship contribution statement

**Patrick Joohyun Kim:** Writing – review & editing, Supervision, Resources, Project administration, Funding acquisition, Conceptualization. **Junghyun Choi:** Writing – review & editing, Supervision, Resources, Funding acquisition, Conceptualization. **Sung Beom Cho:** Writing – review & editing, Supervision, Software, Resources, Funding acquisition, Conceptualization. **Han Uk Lee:** Software, Investigation, Formal analysis. **Kwanghyun Kim:** Methodology, Formal analysis, Data curation. **Min Sung Kang:** Writing – original draft, Software, Investigation, Formal analysis, Data curation. **Wootaek Choi:** Writing – review & editing, Writing – original draft, Methodology, Investigation, Formal analysis, Data curation, Conceptualization.

#### Declaration of Competing Interest

The authors declare that they have no known competing financial interests or personal relationships that could have appeared to influence the work reported in this paper.

#### Acknowledgements

This research was supported by the National Research Council of Science & Technology (NST) grant by the Korea government (MSIT) (No. GTL24012–000), and the National R&D Program through the National Research Foundation of Korea (NRF) (RS-2025-02218301), and by the Korea Institute for Advancement of Technology (KIAT), funded by the Ministry of Trade, Industry and Energy (MI) (RS-2024-00419967).

#### Appendix A. Supporting information

Supplementary data associated with this article can be found in the online version at [doi:10.1016/j.nanoen.2025.111444](https://doi.org/10.1016/j.nanoen.2025.111444).

#### Data availability

Data will be made available on request.

#### References

- [1] R. Schmuck, R. Wagner, G. Hörpel, T. Placke, M. Winter, Performance and cost of materials for lithium-based rechargeable automotive batteries, *Nat. Energy* 3 (2018) 267–278, <https://doi.org/10.1038/s41560-018-0107-2>.
- [2] M. Wan, S. Kang, L. Wang, H.-W. Lee, G.W. Zheng, Y. Cui, Y. Sun, Mechanical rolling formation of interpenetrated lithium metal/lithium tin alloy foil for ultrahigh-rate battery anode, *Nat. Commun.* 11 (2020) 829, <https://doi.org/10.1149/1.3495992>.
- [3] C. Fang, J. Li, M. Zhang, Y. Zhang, F. Yang, J.Z. Lee, M.-H. Lee, J. Alvarado, M. A. Schroeder, Y. Yang, Quantifying inactive lithium in lithium metal batteries, *Nature* 572 (2019) 511–515, <https://doi.org/10.1038/j.commatsci.2012.10.028>.
- [4] J.-M. Tarascon, M. Armand, Issues and challenges facing rechargeable lithium batteries, *nature* 414 (2001) 359–367, <https://doi.org/10.1038/35104644>.
- [5] L. Chen, T. Gu, J. Mi, Y. Li, K. Yang, J. Ma, X. An, Y. Jiang, D. Zhang, X. Cheng, Homogeneous polymer-ionic solvate electrolyte with weak dipole-dipole interaction enabling long cycling pouch lithium metal battery, *Nat. Commun.* 16 (2025) 3517, <https://doi.org/10.1038/s41467-025-58627-3>.
- [7] W. Choi, M. Park, S. Woo, H. Kim, M.S. Kang, J. Choi, S.B. Cho, T. Kim, P.J. Kim, Towards ultra-stable and dendrite-suppressed Li-metal batteries: Ion-regulating graphene-modified separators, *Carbon* 230 (2024) 119576, <https://doi.org/10.1016/j.carbon.2024.119576>.
- [8] P.J. Kim, K. Kim, V.G. Pol, Uniform metal-ion flux through interface-modified membrane for highly stable metal batteries, *Electrochim. Acta* 283 (2018) 517–527, <https://doi.org/10.1016/j.electacta.2018.06.177>.
- [9] Q. Li, S. Zhu, Y. Lu, 3D porous cu current collector/Li-metal composite anode for stable lithium-metal batteries, *Adv. Funct. Mater.* 27 (2017) 1606422, <https://doi.org/10.1002/adfm.201606422>.
- [10] C.-P. Yang, Y.-X. Yin, S.-F. Zhang, N.-W. Li, Y.-G. Guo, Accommodating lithium into 3D current collectors with a submicron skeleton towards long-life lithium metal anodes, *Nat. Commun.* 6 (2015) 8058, <https://doi.org/10.1038/ncomms9058>.
- [11] H. Zhang, X. Liao, Y. Guan, Y. Xiang, M. Li, W. Zhang, X. Zhu, H. Ming, L. Lu, J. Qiu, Lithiophilic-lithiophobic gradient interfacial layer for a highly stable lithium metal anode, *Nat. Commun.* 9 (2018) 3729, <https://doi.org/10.1038/s41467-018-06126-z>.
- [12] K. Liu, A. Pei, H.R. Lee, B. Kong, N. Liu, D. Lin, Y. Liu, C. Liu, P.-c Hsu, Z. Bao, Lithium metal anodes with an adaptive “solid-liquid” interfacial protective layer, *J. Am. Chem. Soc.* 139 (2017) 4815–4820, <https://doi.org/10.1021/jacs.6b13314>.
- [13] Y. Zhang, B. Liu, E. Hitz, W. Luo, Y. Yao, Y. Li, J. Dai, C. Chen, Y. Wang, C. Yang, A carbon-based 3D current collector with surface protection for li metal anode, *Nano Res* 10 (2017) 1356–1365, <https://doi.org/10.1007/s12274-017-1461-2>.
- [14] F. Pei, A. Fu, W. Ye, J. Peng, X. Fang, M.-S. Wang, N. Zheng, Robust lithium metal anodes realized by lithiophilic 3D porous current collectors for constructing high-energy lithium-sulfur batteries, *ACS Nano* 13 (2019) 8337–8346, <https://doi.org/10.1021/acsnano.9b03784>.
- [15] K. Dujeanic-Stephane, M. Gupta, A. Kumar, V. Sharma, S. Pandit, P. Bocchetta, Y. Kumar, The effect of modifications of activated carbon materials on the capacitive performance: surface, microstructure, and wettability, *J. Compos. Sci.* 5 (2021) 66, <https://doi.org/10.3390/jcs5030066>.
- [16] J. Feng, Z. Guo, Wettability of graphene: from influencing factors and reversible conversions to potential applications, *Nanoscale Horiz.* 4 (2019) 339–364, <https://doi.org/10.1039/c8nh00348c>.
- [17] P. Shi, T. Li, R. Zhang, X. Shen, X.B. Cheng, R. Xu, J.Q. Huang, X.R. Chen, H. Liu, Q. Zhang, Lithiophilic LiC6 layers on carbon hosts enabling stable li metal anode in working batteries, *Adv. Mater.* 31 (2019) 1807131, <https://doi.org/10.1002/adma.201807131>.
- [18] C. Jin, O. Sheng, J. Luo, H. Yuan, C. Fang, W. Zhang, H. Huang, Y. Gan, Y. Xia, C. Liang, 3D lithium metal embedded within lithiophilic porous matrix for stable lithium metal batteries, *Nano Energy* 37 (2017) 177–186, <https://doi.org/10.1016/j.nanoen.2017.05.015>.
- [19] X. Feng, H.-H. Wu, B. Gao, M. Świętłowski, X. He, Q. Zhang, Lithiophilic N-doped carbon bowls induced li deposition in layered graphene film for advanced lithium metal batteries, *Nano Res.* 15 (2022) 352–360, <https://doi.org/10.1007/s12274-021-3482-0>.
- [20] G. Huang, J. Han, F. Zhang, Z. Wang, H. Kashani, K. Watanabe, M. Chen, Lithiophilic 3D nanoporous nitrogen-doped graphene for dendrite-free and ultrahigh-rate lithium-metal anodes, *Adv. Mater.* 31 (2019) 1805334, <https://doi.org/10.1002/adma.201805334>.
- [21] Q. Lu, Y. Jie, X. Meng, A. Omar, D. Mikhailova, R. Cao, S. Jiao, Y. Lu, Y. Xu, Carbon materials for stable li metal anodes: challenges, solutions, and outlook, *Carbon Energy* 3 (2021) 957–975, <https://doi.org/10.1002/cey2.147>.
- [22] J. Duan, Y. Zheng, W. Luo, W. Wu, T. Wang, Y. Xie, S. Li, J. Li, Y. Huang, Is graphite lithiophilic or lithiophilic? *Natl. Sci. Rev.* 7 (2020) 1208–1217, <https://doi.org/10.1093/nsr/nwz222>.
- [23] J. Kim, J. Choi, P.J. Kim, A new approach to stabilize the electrochemical performance of li metal batteries through the structure alteration of CNT scaffolds, *Carbon* 203 (2023) 426–435, <https://doi.org/10.1016/j.carbon.2022.11.101>.
- [24] P.E. Blöchl, Projector augmented-wave method, *Phys. Rev. B* 50 (1994) 17953, <https://doi.org/10.1103/PhysRevB.50.17953>.
- [25] G. Kresse, J. Furthmüller, Efficient iterative schemes for ab initio total-energy calculations using a plane-wave basis set, *Phys. Rev. B* 54 (1996) 11169, <https://doi.org/10.1103/PhysRevB.54.11169>.
- [26] J.P. Perdew, K. Burke, M. Ernzerhof, Generalized gradient approximation made simple, *Phys. Rev. Lett.* 77 (1996) 3865, <https://doi.org/10.1103/PhysRevLett.78.1396>.
- [27] A.P. Thompson, H.M. Aktulga, R. Berger, D.S. Bolintineanu, W.M. Brown, P. S. Crozier, P.J. In't veld, A. Kohlmeyer, S.G. Moore, T.D. Nguyen, LAMMPS-a flexible simulation tool for particle-based materials modeling at the atomic, meso,

- and continuum scales, *Comput. Phys. Commun.* 271 (2022) 108171, <https://doi.org/10.1016/j.cpc.2021.108171>.
- [28] K. Chenoweth, A.C. Van Duin, W.A. Goddard, ReaxFF reactive force field for molecular dynamics simulations of hydrocarbon oxidation, *J. Phys. Chem. A* 112 (2008) 1040–1053, <https://doi.org/10.1021/jp709896w>.
- [29] T.P. Senftle, S. Hong, M.M. Islam, S.B. Kyllasa, Y. Zheng, Y.K. Shin, C. Junkermeier, R. Engel-Herbert, M.J. Janik, H.M. Aktulga, The ReaxFF reactive force-field: development, applications and future directions, *npj Comput. Mater.* 2 (2016) 1–14, <https://doi.org/10.1038/npjcompumats.2015.11>.
- [30] S.P. Ong, W.D. Richards, A. Jain, G. Hautier, M. Kocher, S. Cholia, D. Gunter, V. L. Chevrier, K.A. Persson, G. Ceder, Python materials genomics ( pymatgen): a robust, open-source python library for materials analysis, *Comput. Mater. Sci.* 68 (2013) 314–319, <https://doi.org/10.1016/j.commatsci.2012.10.028>.
- [31] W.G. Hoover, Canonical dynamics: equilibrium phase-space distributions, *Phys. Rev. A* 31 (1985) 1695, <https://doi.org/10.1103/PhysRevA.31.1695>.
- [32] R. Kumar, A. Parashar, Dislocation assisted crack healing in h-BN nanosheets, *Phys. Chem. Chem. Phys.* 19 (2017) 21739–21747, <https://doi.org/10.1039/c7cp04455k>.
- [33] A. Stukowski, Visualization and analysis of atomistic simulation data with OVITO—the open visualization tool, *Model. Simul. Mater. Sci. Eng.* 18 (2009) 015012, <https://doi.org/10.1088/0965-0393/18/1/015012>.
- [34] H. Hermann, T. Schubert, W. Gruner, N. Mattern, Structure and chemical reactivity of ball-milled graphite, *Nanostruct. Mater.* 8 (1997) 215–229, [https://doi.org/10.1016/S0965-9773\(97\)00010-X](https://doi.org/10.1016/S0965-9773(97)00010-X).
- [35] F.T.L. Muniz, M.R. Miranda, C. Morilla dos Santos, J.M. Sasaki, The scherrer equation and the dynamical theory of X-ray diffraction, *Found. Crystallogr.* 72 (2016) 385–390, <https://doi.org/10.1107/S205327331600365X>.
- [36] A. Milev, M. Wilson, G.K. Kannangara, N. Tran, X-ray diffraction line profile analysis of nanocrystalline graphite, *Mater. Chem. Phys.* 111 (2008) 346–350, <https://doi.org/10.1016/j.matchemphys.2008.04.024>.
- [37] K.N. Kudin, B. Ozbas, H.C. Schniepp, R.K. Prud'Homme, I.A. Aksay, R. Car, Raman spectra of graphite oxide and functionalized graphene sheets, *Nano Lett.* 8 (2008) 36–41, <https://doi.org/10.1021/nl071822y>.
- [38] S. Mahanta, U. Balaji, S. Pradhan, S. Suman, K. Sankaran, Towards High-quality graphite oxide from graphite–systemization of the balance in oxidative and mechanical forces for yield enhancement, *Chem. Eng. Sci.* 259 (2022) 117815, <https://doi.org/10.1016/j.ces.2022.117815>.
- [39] A. Verma, A. Parashar, Molecular dynamics based simulations to study the fracture strength of monolayer graphene oxide, *Nanotechnol* 29 (2018) 115706, <https://doi.org/10.1088/1361-6528/aaa8bb>.
- [40] Y. Wang, Z. Fan, P. Qian, T. Ala-Nissila, M.A. Caro, Structure and pore size distribution in nanoporous carbon, *Chem. Mater.* 34 (2022) 617–628, <https://doi.org/10.1021/acs.chemmater.1c03279>.
- [41] T. Hao, Tap density equations of granular powders based on the rate process theory and the free volume concept, *Soft Matter* 11 (2015) 1554–1561, <https://doi.org/10.1039/c4sm02472a>.
- [42] C. Chang, R.L. Powell, Effect of particle size distributions on the rheology of concentrated bimodal suspensions, *J. Rheol.* 38 (1994) 85–98, <https://doi.org/10.1122/1.550497>.
- [43] H. Yildirim, A. Kinaci, Z.-J. Zhao, M.K. Chan, J.P. Greeley, First-principles analysis of defect-mediated li adsorption on graphene, *ACS Appl. Mater. Interfaces* 6 (2014) 21141–21150, <https://doi.org/10.1021/am506008w>.
- [44] M. Wang, J. Wang, J. Xiao, N. Ren, B. Pan, C.-s Chen, C.-h Chen, Introducing a pseudocapacitive lithium storage mechanism into graphite by defect engineering for fast-charging lithium-ion batteries, *ACS Appl. Mater. Interfaces* 14 (2022) 16279–16288, <https://doi.org/10.1021/acsami.2c02169>.
- [45] J. Tian, D. Cao, X. Zhou, J. Hu, M. Huang, C. Li, High-capacity Mg–organic batteries based on nanostructured rhodizonate salts activated by Mg–Li dual-salt electrolyte, *ACS Nano* 12 (2018) 3424–3435, <https://doi.org/10.1021/acsnano.7b09177>.
- [46] T. Liu, C. Zhu, T. Kou, M.A. Worsley, F. Qian, C. Condes, E.B. Duoss, C. M. Spadaccini, Y. Li, Ion intercalation induced capacitance improvement for graphene-based supercapacitor electrodes, *ChemNanoMat* 2 (2016) 635–641, <https://doi.org/10.1002/cnma.201600107>.
- [47] B.K. Kanchan, P. Randive, Investigation on capacity extension through non-uniform anode microstructure in lithium-ion battery, *Int. J. Heat. Mass Transf.* 214 (2023) 124413, <https://doi.org/10.1016/j.ijheatmasstransfer.2023.124413>.
- [48] V. Ramadesigan, R.N. Methkar, F. Latinwo, R.D. Braatz, V.R. Subramanian, Optimal porosity distribution for minimized ohmic drop across a porous electrode, *J. Electrochim. Soc.* 157 (2010) A1328, <https://doi.org/10.1149/1.3495992>.
- [49] H. Fu, X. Bao, M. He, J. Xu, Z. Miao, M. Ding, J. Liu, C. Jia, Defect-rich graphene skin modified carbon felt as a highly enhanced electrode for vanadium redox flow batteries, *J. Power Sources* 556 (2023) 232443, <https://doi.org/10.1016/j.jpowsour.2022.232443>.
- [50] Y. Zhou, X. Ning, Improving wettability at positive electrodes to enhance the cycling stability of Bi-Based liquid metal batteries, *Small* 20 (2024) 2304528, <https://doi.org/10.1002/smll.202304528>.
- [51] B.R. Pant, Y. Ren, Y. Cao, Dendrite growth and dead lithium formation in lithium metal batteries and mitigation using a protective layer: a Phase-Field study, *ACS Appl. Mater. Interfaces* 16 (2024) 56947–56956, <https://doi.org/10.1021/acsmi.4c08605>.
- [52] X. Duan, B. Li, J. Li, X. Gao, L. Wang, J. Xu, Quantitative understanding of lithium deposition-stripping process on graphite anodes of lithium-ion batteries, *Adv. Energy Mater.* 13 (2023) 2203767, <https://doi.org/10.1002/aenm.202203767>.
- [53] L. Guan, H. Hu, L. Li, Y. Pan, Y. Zhu, Q. Li, H. Guo, K. Wang, Y. Huang, M. Zhang, Intrinsic defect-rich hierarchically porous carbon architectures enabling enhanced capture and catalytic conversion of polysulfides, *ACS Nano* 14 (2020) 6222–6231, <https://doi.org/10.1021/acsnano.0c02294>.
- [54] C. Wang, J. Huang, L. Cao, J. Li, C. He, H. Li, J. Tian, K. Kajiyoshi, Intrinsic defects promote rapid conversion of polysulfides on carbon surface to achieve high rate performance, *Carbon* 183 (2021) 899–911, <https://doi.org/10.1016/j.carbon.2021.07.071>.
- [55] C.-Y. Fan, H.-Y. Yuan, H.-H. Li, H.-F. Wang, W.-L. Li, H.-Z. Sun, X.-L. Wu, J.-P. Zhang, The effective design of a polysulfide-trapped separator at the molecular level for high energy density Li–S batteries, *ACS Appl. Mater. Interfaces* 8 (2016) 16108–16115, <https://doi.org/10.1021/acsmi.6b04578>.
- [56] S.A. Abbas, J. Ding, S.H. Wu, J. Fang, K.M. Boopathi, A. Mohapatra, L.W. Lee, P.-C. Wang, C.-C. Chang, C.W. Chu, Modified separator performing dual physical/chemical roles to inhibit polysulfide shuttle resulting in ultrastable Li–S batteries, *Acs Nano* 11 (2017) 12436–12445, <https://doi.org/10.1021/acsnano.7b06478>.
- [57] S.H. Chung, A. Manthiram, Bifunctional separator with a light-weight carbon-coating for dynamically and statically stable lithium-sulfur batteries, *Adv. Funct. Mater.* 24 (2014) 5299–5306, <https://doi.org/10.1002/adfm.201400845>.
- [58] Z.A. Ghazi, X. He, A.M. Khattak, N.A. Khan, B. Liang, A. Iqbal, J. Wang, H. Sin, L. Li, Z. Tang, MoS<sub>2</sub>/celgard separator as efficient polysulfide barrier for long-life lithium–sulfur batteries, *Adv. Mater.* 29 (2017) 1606817, <https://doi.org/10.1002/adma.201606817>.



**Woontaeck Choi** received his B.S. degree from Kyungpook National University in 2024. His research focuses on the engineering of current collectors for lithium metal batteries.



**Min Sung Kang** received his B.S. degree from Myongji University in 2022. His research focuses on Li-ion batteries, energy harvesting and crystallization.



**Kwanghyun Kim** received his B.S. degree from Keimyung University in 2022 and M.S. degree from Kyungpook National University in 2024. His research focuses on the engineering of current collectors for lithium metal batteries.



**Han Uk Lee** received his B.S. degree from Gyeongsang National University in 2022. His research focuses on Li-ion batteries based on computational simulation.



**Prof. Sung Beom Cho** is currently an Assistant Professor at Ajou University, where he leads a research group specializing in computational materials science and materials informatics. He received his Ph.D. in 2017 from Hanyang University and conducted postdoctoral research at Washington University between 2017 and 2018. From 2018–2022, he worked as a Senior Researcher at KICET, contributing to industrial projects focused on electronic and energy systems through the application of various computational techniques. His research is centered on using computational approaches to analyze and predict the properties and behavior of diverse material systems.



**Prof. Patrick Joohyun Kim** is an Associate Professor in the School of Chemical Engineering and Applied Chemistry at Kyungpook National University, South Korea. He received his Ph.D. in 2017 from Hanyang University and carried out postdoctoral research at the School of Chemical Engineering at Purdue University between 2017 and 2019. From 2019–2021, he worked as a neutron beamline scientist at the NIST Center for Neutron Research, part of the National Institute of Standards and Technology (NIST). He joined Kyungpook National University in 2021. His research centers on the synthesis, functionalization, and characterization of carbon nano-materials for advanced energy storage applications.



**Prof. Junghyun Choi** is an Assistant Professor in the School of Chemical, Biological, and Battery Engineering at Gachon University. He earned his Ph.D. in Energy Engineering from Hanyang University in 2016. He has held research positions at the Samsung Advanced Institute of Technology (SAIT), Samsung SDI, and the Korea Institute of Ceramic Engineering and Technology (KICET). His research interests lie in materials development and processing technologies for high-energy-density energy storage systems.